Received 18 January 2023; revised 11 March 2023; accepted 29 March 2023. Date of publication 10 April 2023; date of current version 25 April 2023.

Digital Object Identifier 10.1109/OJCOMS.2023.3265013

Combined Radar and Communications With Phase-Modulated Frequency Permutations

TIAN HAN [1] (Graduate Student Member, IEEE), RAJITHA SENANAYAKE [1] (Member, IEEE), PETER SMITH [2] (Fellow, IEEE), JAMIE EVANS [1] (Senior Member, IEEE), WILLIAM MORAN [1] (Member, IEEE), AND ROBIN EVANS [1] (Life Fellow, IEEE)

[1]Department of Electrical and Electronic Engineering, The University of Melbourne, VIC 3010, Australia

[2]School of Mathematics and Statistics, Victoria University of Wellington, Wellington 6012, New Zealand

CORRESPONDING AUTHOR: T. HAN (e-mail: tianh2@student.unimelb.edu.au)

This work was supported in part by the Australian Research Council (ARC) through the Discovery Project under Grant DP200103625.

ABSTRACT This paper focuses on the combined radar and communications problem and conducts a thorough analytical investigation on the effect of phase and frequency change on the communication and sensing functionality. First, we consider the classical stepped frequency radar waveform and modulate data using M-ary phase shift keying (MPSK). Two important analytical tools in radar waveform design, namely the ambiguity function (AF) and the Fisher information matrix (FIM) are derived, based on which, we make the important conclusion that MPSK modulation has a negligible effect on radar local accuracy. Next, we extend the analysis to incorporate frequency permutations and propose a new signalling scheme in which the mapping between incoming data and waveforms is performed based on an efficient combinatorial transform called the Lehmer code. We also provide an efficient communications receiver based on a modified Hungarian algorithm. From the communications perspective, we consider the optimal maximum likelihood (ML) detector and derive the union bound and nearest neighbour approximation on the block error probability. From the radar sensing perspective, we discuss the broader structure of the waveform based on the AF derivation and quantify the radar local accuracy based on the FIM. Extensive numerical examples are provided to illustrate the accuracy of our results.

INDEX TERMS Joint communications and radar, maximum likelihood, ambiguity function, Fisher information matrix.

I. INTRODUCTION

THE INTEGRATION of radar sensing and communication is a promising design paradigm in which sensing and communication functionalities share the same hardware and spectrum resources. Traditionally, communications and radar sensing were designed separately to focus on domain specific challenges. However, as communication systems start to use the millimeter-wave (mmWave) frequency band which is traditionally used in radar, there has been an increasing amount of research interest in the integration of the two functionalities [1], [2], [3], [4], [5], [6], [7], [8]. Such joint systems can contribute to reducing the system cost and power consumption, as well as alleviating concerns for spectrum congestion [9].

A key aspect of the co-existence of these two functions in an integrated system is the design of a joint waveform that is capable of transmitting information and performing radar sensing simultaneously. This convergence could be achieved based on different approaches as discussed in [4], [5], [6], [7], [10], [11], [12]. For example, some research focuses on embedding information into traditional radar waveforms for joint application. In [13], the traditional linear frequency modulated (LFM) waveform is considered for data transmission. However, the communication symbol rate corresponds to the chirp rate only, which is much lower than the symbol rate that can be achieved by a communication system with the same bandwidth. In [14], a phase-attached radar-communications (PARC) framework is extended to

a frequency modulated continuous-wave (FMCW) implementation as a means to realise both functions. Stretch processing is employed such that large bandwidth radar operation and fine range resolution can be achieved. In [15], information sequences are implemented using continuous phase modulation (CPM) and phase-attached to a polyphase-coded frequency-modulated (PCFM) fixed radar waveform. The adjustable parameters provide control of the range side-lobe modulation (RSM) by trading off bit error rate (BER) and/or data throughput. Using frequency-hopping (FH) multiple-input multiple-output (MIMO) radar for dual-function radar-communication (DFRC) has increased the symbol rate to multiples of pulse repetition frequency by modulating information into fast time subpulses [16], [17], [18], [19]. In [18], a unique FH-MIMO waveform based DFRC scheme is proposed in order to address issues including channel estimation and synchronisation in multi-path channels. In [17], the presented FH-MIMO radar based DFRC frameworks combine various existing signalling strategies including phase shift keying (PSK), FH code selection and FH code permutations, in order to further boost the communication data rates. However, the FH code selection and permutation based methods only consider the orthogonality between waveforms transmitted by different antennas. A degradation in the radar performance can occur if there is a repetition of frequencies in the time domain subpulses of the waveform transmitted by a single antenna.

Research is also underway on the opposite design pattern, i.e., using traditional communication waveforms for radar sensing. The use of orthogonal frequency division multiplexing (OFDM) waveforms for the joint system was considered in [20], [21], [22]. In [21], a wideband OFDM based waveform is presented and the high range resolution processing is derived. Furthermore, the impact of Doppler modulation on the processing is inspected to give recommendations of the OFDM parameters. In [22], the design of a power minimisation-based robust OFDM radar waveform is considered. However, due to the large number of subcarriers in the OFDM waveform it introduces high peak-to-average power ratio (PAPR). This makes the approach challenging for typical radar operation since it requires power amplifiers with a large linear range. Taking a different approach, in [23], the IEEE 802.11ad-based waveform which is traditionally used for wireless local area networks (WLANs) is proposed for long-range radar (LRR) applications in the 60 GHz unlicensed band. The preamble of this waveform, which consists of Golay complementary sequences with good correlation properties, is exploited to make it suitable for radar applications. In [24], a virtual waveform design based on IEEE 802.11ad is proposed for an adaptive mmWave joint communications and radar (JCR) system. The system transmits a few non-uniformly placed preambles to enhance the velocity estimation accuracy, at the cost of a small reduction in the communication data rate. In [25], a self-interference-resistant IEEE 802.11ad based JCR framework is developed. The Golay sequences and a novel pilot signal design are leveraged to combat self-interference in different sensing scenarios. Though IEEE 802.11ad-based JCR has data rate competitive to pure communications systems, the radar sensing ability is limited due to the limitation on the length of the preambles.

Existing methods show that one main challenge of embedding information into conventional radar waveforms is the limited data rate due to the lack of randomness. Boosting the rate is possible, but it requires the randomisation of parameters that affect the radar estimation accuracy and this can cause degradation in radar performance. Taking a different approach to the aforementioned papers, here, we focus on embedding data into the conventional stepped frequency radar waveform by randomising the parameters that have little effect on radar performance, which can potentially increase the data rate with an insignificant impact on the radar performance. We consider the hybrid use of frequency permutations and PSK, and conduct a rigorous theoretical analysis on the effect of phase and frequency modulation on the radar sensing functionality, which, to the best of our knowledge, is an open research problem.

Stepped frequency waveforms are commonly used in radar applications. A stepped frequency waveform has multiple subpulses, each with a constant frequency tone, but the frequencies of different subpulses are equally separated by a constant step Δf Hz. Examples of stepped frequency radar waveforms include the linear stepped frequency waveform [26] and Costas coded waveform [27]. Phase coding is one of the early methods for pulse compression in radar applications [27]. Chirp like polyphase codes, such as Frank codes [28], have properties of low autocorrelation side-lobe levels and good Doppler tolerance. In [29], modified versions of Frank codes, namely P1 and P2 codes, are proposed. Compared to Frank codes, P1 and P2 codes are more tolerant of receiver band-limiting prior to pulse compression. All of these waveforms, however, maintain a strict sequence of phase values carefully designed to achieve the best radar performance, which are not suitable for joint operation due to the lack of randomness.

In this paper, we change the phase and frequency of the conventional stepped frequency radar waveform to form a new waveform that is suitable for both data transmission and radar sensing. First, we focus on the phase change by incorporating PSK modulation to the classical stepped frequency radar waveform. Next, we extend this by combining the frequency permutation based modulation introduced in [30], [31] with the phase modulation to formulate a new modulation scheme. The joint use of both phase and frequency, solely for communication purposes, has recently been analysed in [32]. They proposed a novel M-ary frequency-phase keying modulation, in which the frequency and phase are operated in a discrete, slot-by-slot manner. In our proposed modulation method, the frequency is also changed in a discrete manner but based on the selected permutation, while the phase is changed based on PSK modulation. This allows us to use phase and frequency

independently to modulate data and as a result transmit more data between nodes. Furthermore, it has been shown in [31] that the frequency permutation based joint waveform has good ambiguity function (AF) performance on average. As will be discussed in this paper, incorporating phase modulation on top of the frequency permutation has limited impact on the AF, which makes the increase in data rate almost free of charge in terms of radar performance. We provide a rigorous theoretical analysis of the proposed waveform, both in terms of communication performance and radar performance, and make comparisons with other proposed approaches such as [31], which only consider frequency modulation. The main contributions of this paper are as follows:

- First, we analyse the effect of phase modulation on the radar performance of the linear stepped frequency waveform. More specifically, we derive the AF and discuss its broader structure and side-lobe levels. We also derive approximate expressions for the Cramer-Rao lower bounds (CRLBs) on the delay and Doppler estimation errors based on the Fisher information matrix (FIM), and provide a detailed evaluation of the local accuracy. Based on the analytic tools, we analyse the impact of incorporating phase modulation into the traditional linear stepped frequency waveform on radar estimation accuracy.
- Next, we combine phase modulation and permutation of the frequency tones to propose a novel integrated radar and communication waveform. We present a new signalling scheme which allows more data to be transmitted and provide an efficient implementation for the mapping between the incoming data and the corresponding waveform based on a combinatorial transform called the Lehmer code. We derive the AF and propose a novel way of analysing the overall AF performance by approximating the average AF of random frequency and phase modulated waveforms using a Rician distribution. We also derive the FIM and approximations to the CRLBs, based on which the cost of embedding data using phase modulation into frequency permutation based waveforms is analysed. We make a thorough performance comparison to the work in [31] which, in contrast to the work here, only uses frequency permutations for the data modulation.
- From a communications perspective, we consider maximum likelihood (ML) detection and analyse the error probability of the receiver in different wireless communication models. As we proposed a novel modulation scheme, the derivation of its error probability performance is new and challenging. For additive white Gaussian noise (AWGN) channels and correlated Rician fading channels, we derive the union bound as well as the nearest neighbour approximation to the block error probability. In addition, we derive a new upper bound on the block error probability under the correlated Rayleigh fading model. To deal with the high complexity of an exhaustive search in ML detection, we provide an efficient implementation of the optimal ML receiver based on a modified Hungarian algorithm.

Extensive numerical examples are provided to illustrate the accuracy of our results.

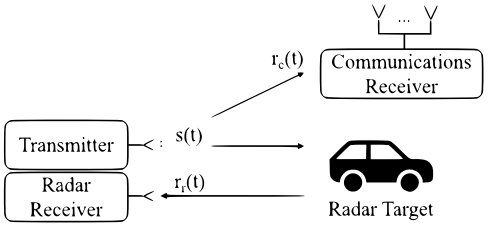

FIGURE 1. The JCR system model.

II. PROBLEM FORMULATION

A. SYSTEM MODEL

We consider a JCR system model, as illustrated in Fig. 1, where the transmitter sends a common waveform to both the radar target and the communications receiver. The signal reflected from the radar target is received and processed by the radar receiver, which is co-located with the transmitter, to estimate the range and relative velocity of the target. The signal received at the communications receiver is processed to detect the transmitted information.

First, let us focus on the classical stepped frequency radar waveform with linearly increasing frequency tones. The complex envelope of such a stepped frequency radar waveform with L subpulses of length T can be given by

$$s(t) = \sqrt{\frac{E}{LT}} \sum_{l=0}^{L-1} s_p(t - lT) \exp\left(j2\pi f_l (t - lT)\right), \qquad (1)$$

where the energy of the waveform $E = \int_0^{LT} |s(t)|^2 dt$ and $s_p(t)$ is a simple rectangular pulse

$$s_p(t) = \begin{cases} 1, & 0 \le t \le T \\ 0, & \text{otherwise.} \end{cases}$$

We also assume that the frequency tones are in ascending order and the difference between two successive frequency tones is $\Delta f = n/T$, where n is a positive integer. As such, the frequencies are orthogonal to each other and the frequency tone of the l-th subpulse can be expressed as

$$f_l = f_0 + n(l-1)/T. \qquad (2)$$

In the current paper, we investigate novel methods of modulating the phase and frequency without causing significant changes to radar sensing functionality. We keep the amplitude fixed because constant amplitude is extremely important for the efficient use of the power amplifiers in radar operation [26].

B. RADAR PERFORMANCE MEASURES

In this paper, we focus on AF and FIM, the two key analytical tools used in radar waveform design. For completeness, we have provided the definitions of these tools as follows.

The AF of a waveform describes the output of a matched filter when the signal input to the radar receiver is delayed and Doppler shifted by certain amounts. Based on [26, eq. (4.30)], the complex AF of the waveform $s(t)$ in (1) can be expressed as

$$\hat{A}(\tau, \omega) = \int_{-\infty}^{\infty} s(t)s^*(t-\tau)e^{-j\omega t}dt, \tag{3}$$

where τ is the time delay to the expected matched filter peak output, and ω is the Doppler mismatch between the Doppler shift of the received signal and that for which the filter is designed. Then the AF is defined as the magnitude of the complex AF and is given by

$$A(\tau, \omega) = \left|\hat{A}(\tau, \omega)\right|. \tag{4}$$

The AF provides a measure of the degree of similarity between the transmitted waveform and its time and frequency shifted version [33]. The local accuracy can be analysed based on the shape of the AF around the origin, while the ambiguity can be studied by the AF side-lobe levels.

The FIM for the delay and Doppler shift estimations provide a more detailed evaluation of the local accuracy of the waveform [33]. Consider the complex envelope of the radar received signal reflected by a single target, which can be written as

$$r_r(t) = \tilde{b}s(t-\tau)e^{j\omega t} + n(t), \tag{5}$$

where τ and ω are the target delay and Doppler shift to be estimated, $\tilde{b}$ is a complex Gaussian random variable with zero mean and unit variance and $n(t)$ represents the baseband complex additive white Gaussian noise process with zero mean and power spectrum density N_0 [33, eq. (10.5)]. The Rayleigh fading variable, $\tilde{b}$, models the reflection from a target with multiple reflecting surfaces. The FIM for τ and ω is defined as

$$\boldsymbol{J} = \begin{bmatrix} J_{11} & J_{12} \\ J_{21} & J_{22} \end{bmatrix}, \tag{6}$$

where subscript 1 denotes τ and subscript 2 denotes ω. Using [33, eq. (10.63)-(10.65)], the elements of $\boldsymbol{J}$ can be written as

$$J_{11} = C\left[\overline{\omega^2} - \bar{\omega}^2\right], \tag{7}$$

$$J_{12} = J_{21} = C[\overline{\omega\tau} - \bar{\omega}\bar{\tau}], \tag{8}$$

$$J_{22} = C\left[\overline{\tau^2} - \bar{\tau}^2\right], \tag{9}$$

where $C = \frac{2}{N_0(1+N_0)}$, $\overline{\omega^2}$, $\overline{\omega\tau}$ and $\overline{\tau^2}$ are given in [33, eq. (10.67)-(10.69)], respectively. Note that $\bar{\omega}$ and $\bar{\tau}$ can be calculated by replacing ω^2 with ω in [33, eq. (10.67)] and replacing u^2 by u in [33, eq. (10.69)], respectively. Based on the FIM elements we can derive the CRLBs on the delay and Doppler estimation errors.

The two performance measures, i.e., the AF and the FIM discussed above, focus on parameter estimation problems. Another important function of radar is the detection of the existence of the target. Nevertheless, this problem is less of interest for our proposed waveform. To be more specific, since we do not consider amplitude modulation, the energy contained in all possible waveforms is the same. Therefore, the communication modulation has an insignificant impact on the detection probability, especially when the commonly used energy detector is considered.

C. RADAR SENSING OPERATION

As illustrated in Fig. 1, from the radar application perspective we adopt a conventional mono-static radar system. More specifically, the transmitter and the radar receiver are co-located such that the radar receiver knows the transmitted waveform. Therefore, the radar operation is exactly the same as a traditional radar system, with the only difference being the randomisation of the transmitted waveform. The transmitter sends a waveform based on random data bits and it is reflected back by the target. The radar receiver correlates the received signal with the transmitted waveform to find the range and Doppler of the target. It is important to note that even though the transmitted waveform is generated based on random data bits, it does not interrupt the radar operation since the radar receiver knows the selected waveform.

Next, we give a brief introduction to the delay-Doppler estimator at the radar receiver. Given the radar channel model in (5), the continuous-time maximum likelihood (ML) delay-Doppler estimator is discussed in [33, Ch. 10.1]. Generally speaking, it makes the delay and Doppler estimations by maximising the outputs of the matched filters matched to waveforms with different Doppler shifts, which can be expressed as

$$\left(\hat{\tau}, \hat{\omega}\right) = argmax_{(\bar{\tau},\bar{\omega})}\left\{\left|\int_{-\infty}^{\infty} r_r(t)s^*(t-\bar{\tau})e^{-j\bar{\omega}t}dt\right|^2\right\}, \tag{10}$$

where $\hat{\tau}$ and $\hat{\omega}$ are estimations of the delay and Doppler shift, respectively. In practice, a discrete-time approximation of (10) is usually considered.

In this paper, we focus on analysing the impact of the proposed modulation method on radar sensing performance. Therefore, estimator-independent analytical tools such as the AF and the FIM are considered as the radar performance measures in this paper. The performance of the estimator in (10) is not the main focus of the paper, and thus will not be included.

III. PHASE MODULATED STEPPED FREQUENCY WAVEFORM

In this section, we introduce phase modulation to embed data into the waveform in (1). Using M PSK to independently modulate the phase in each subpulse, we get a new waveform which can be expressed as

$$s(t) = \sqrt{\frac{E}{LT}}\sum_{l=0}^{L-1} s_p(t-lT)\exp\left(j(2\pi f_l(t-lT) + \theta_l)\right), \tag{11}$$

where $\theta_l \in \{0, 2\pi/M, \ldots, 2\pi(M-1)/M\}$ denotes the phase modulated into the l-th subpulse of the waveform. While adding M PSK allows us to send data, it impacts the radar sensing functionality. Thus, we proceed to analyse the AF and the FIM to discuss the effect of phase change on the radar performance.

A. AMBIGUITY FUNCTION

In order to derive the AF, we normalise the signal energy to one and re-express the waveform in (11) as

$$s(t) = \sqrt{\frac{1}{LT}} \sum_{l=0}^{L-1} s_p(t - lT) \exp\left(j(\omega_l(t - lT) + \theta_l)\right), \quad (12)$$

where $\omega_l = 2\pi f_l$ is the frequency in radians per second.

Substituting (12) into (3) we can write the complex AF of $s(t)$ as

$$\hat{A}(\tau, \omega) = \frac{1}{LT} \sum_{l=0}^{L-1} \sum_{n=0}^{L-1} \int_{-\infty}^{\infty} s_p(s - lT) s_p^*(s - nT - \tau) \times e^{(j(\omega s + \omega_l(t-lT) - \omega_n(s-\tau-nT) + \theta_l - \theta_n))} ds. \quad (13)$$

Writing the complex AF of $s_p(t)$ as $\hat{A}_p(\tau, \omega)$ and rearranging (13) we obtain

$$\hat{A}(\tau, \omega) = \frac{1}{LT} \sum_{l=0}^{L-1} \sum_{n=0}^{L-1} \hat{A}_p(\tau + (n-l)T, \omega - (\omega_n - \omega_l)) \times e^{j(\omega lT + \omega_n(\tau + (n-l)T) + (\theta_l - \theta_n))}, \quad (14)$$

where $\hat{A}_p(\tau, \omega)$ can be written as

$$\hat{A}_p(\tau, \omega) = \begin{cases} \frac{e^{j\omega(\tau+T)} - 1}{j\omega}, & -T < \tau < 0 \\ \frac{e^{j\omega T} - e^{j\omega\tau}}{j\omega}, & 0 \le \tau < T \\ 0, & \text{otherwise.} \end{cases} \quad (15)$$

Next, by taking the magnitude of (14), we can write the AF of the waveform in (12) as

$$A(\tau, \omega) = \left| \frac{1}{LT} \sum_{l=0}^{L-1} \sum_{n=0}^{L-1} \hat{A}_p(\tau + (n-l)T, \omega - (\omega_n - \omega_l)) \times e^{j(\omega lT + \omega_n(\tau + (n-l)T) + (\theta_l - \theta_n))} \right|. \quad (16)$$

The zero-Doppler cut of the AF describes the matched filter output when there is only time delay and no Doppler mismatch. By letting $\omega = 0$ in (16) we can obtain the zero-Doppler cut as

$$A(\tau, 0) = \left| \frac{1}{LT} \sum_{l=0}^{L-1} \sum_{n=0}^{L-1} \hat{A}_p(\tau + (n-l)T, \omega_l - \omega_n) \times e^{j(\omega_n(\tau - (n-l)T) + (\theta_l - \theta_n))} \right|. \quad (17)$$

Similarly, the zero-delay cut of the AF describes the matched filter output when there is no time delay, which can be found by letting $\tau = 0$ in (16) to derive

$$A(0, \omega) = \left| \frac{1}{LT} \sum_{l=0}^{L-1} \sum_{n=0}^{L-1} \hat{A}_p((n-l)T, \omega - (\omega_n - \omega_l)) \times e^{j(\omega lT + \omega_n(n-l)T + (\theta_l - \theta_n))} \right|. \quad (18)$$

Due to the fact that $\hat{A}_p(\tau, \omega)$ in (15) is non-zero only when $-T < \tau < T$, it is obvious that $\hat{A}_p((n-l)T, \omega - (\omega_n - \omega_l))$ is non-zero only when $n = l$. Therefore, the zero-delay cut in (18) can be simplified as

$$A(0, \omega) = \left| \frac{1}{LT} \sum_{l=0}^{L-1} \hat{A}_p(0, \omega) e^{j\omega lT} \right|, \quad (19)$$

which indicates that the zero-delay cut does not change with the phase modulation.

B. FISHER INFORMATION MATRIX AND CRAMER-RAO LOWER BOUNDS

Based on the definition of the FIM in (6) we proceed to derive the elements J_{11}, J_{12}, J_{21} and J_{22} as follows

$$J_{11} \approx \frac{2CB}{LT} \left(L - \sum_{l=0}^{L-2} \cos(\omega_0 T + \theta_l - \theta_{l+1}) \right), \quad (20)$$

$$J_{12} = J_{21} \approx -\frac{CT^2}{2} \sum_{l=0}^{L-1} \omega_l (2l+1), \quad (21)$$

$$J_{22} = \frac{CL^2T^2}{12}, \quad (22)$$

where B is the finite bandwidth occupied by the rectangular pulse shaping function $s_p(t)$. The detailed derivation of J_{11}, J_{22} and J_{12} is not included in the present paper due to page limitations, but the approach follows similar steps as in [34, Appendix C, D and E]. Note that the finite bandwidth B is introduced since $\overline{\omega^2}$ and $\bar{\omega}^2$ do not converge when $s_p(t)$ is a perfect rectangular pulse. The approximation in (20) is derived by neglecting small high order terms in the integrals which vanish when $BT \to \infty$ [34].

The FIM is useful to bound the variance of the individual errors. More specifically, when unbiased estimators are used, the variances of delay and Doppler shift estimation errors are lower bounded by the diagonal elements in $\boldsymbol{J}^{-1}$ [33]. Denoting the CRLBs of the delay estimation and Doppler shift estimation errors as CRLB_τ and CRLB_ω, respectively, their approximate expressions are given in (23) and (24) shown at the bottom of the next page. Note that (23) and (24) can be further simplified based on [33, eq. (10.94), (10.95)] to produce

$$\text{CRLB}_\tau \approx \frac{C^{-1}LT}{2B\left(L - \sum_{l=0}^{L-2} \cos(\omega_0 T + \theta_l - \theta_{l+1})\right)}, \quad (25)$$

$$\text{CRLB}_\omega \approx \frac{12C^{-1}}{L^2T^2}. \quad (26)$$

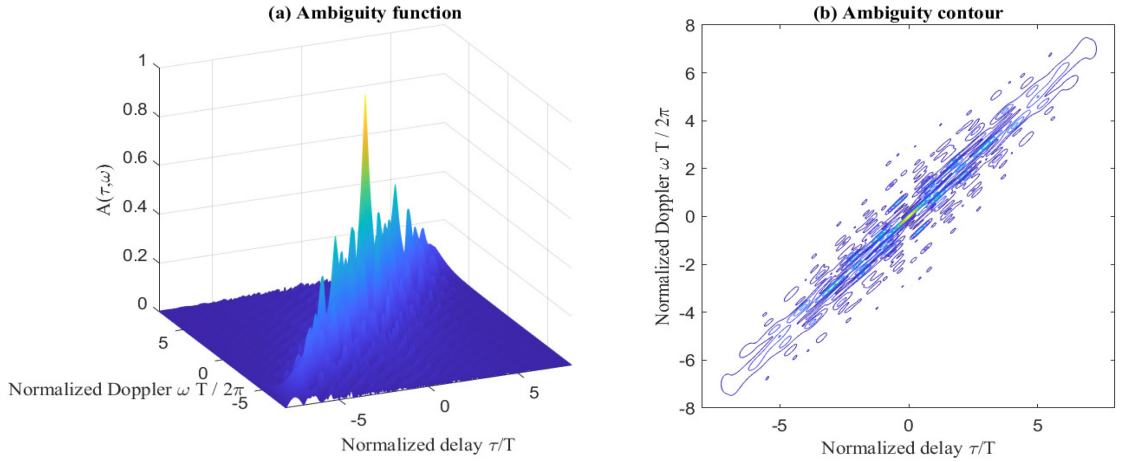

FIGURE 2. The (a) three-dimensional surface plot and (b) contour plot of the AF of a linear stepped frequency and PSK based waveform for $L = 8$ and $M = 4$. The first frequency $f_0 = 0$ Hz and the step $\Delta f = 1/T$ Hz. The phase sequence is [$3\pi/4$, $3\pi/4$, $3\pi/4$, $\pi/2$, $3\pi/4$, $\pi/2$, $\pi/4$, $\pi/2$].

While the simplified expressions in (25) and (26) provide looser bounds compared to (23) and (24), they clearly show the effect of parameters on the estimation errors. The delay estimation error lower bound in (25) is inversely proportional to the product of the finite bandwidth B and the effective bandwidth $1/T$ of a single subpulse. The Doppler shift estimation error lower bound in (26) is inversely proportional to the square of the time duration of the whole waveform LT. To observe the effect of embedding data on local accuracy, we first derive the CRLBs for stepped frequency waveforms without phase modulation by setting $\theta_m = 0$ in (25) and (26), which results in

$$\mathrm{CRLB}_\tau \approx \frac{C^{-1}LT}{2B(L-(L-1)\cos(\omega_0 T))}, \tag{27}$$

$$\mathrm{CRLB}_\omega \approx \frac{12C^{-1}}{L^2T^2}. \tag{28}$$

Comparing the CRLBs in (27) and (28) with those in (25) and (26), it can be found that the phase modulation has exactly no effect on the simplified CRLB_ω while it has some influence on CRLB_τ. Nevertheless, the maximum value (when all $\cos(\cdot)$ terms equal 1) and minimum value (when all $\cos(\cdot)$ terms equal -1) of the simplified CRLB_τ are kept unchanged when phase modulation is introduced. The above discussions are further analysed using numerical examples in Section III-C below.

C. NUMERICAL EXAMPLES

In this section, we provide numerical examples to support the radar performance analyses in Sections III-A and Section III-B. Fig. 2 and Fig. 3 illustrate the AF while Fig. 4 illustrates the CRLBs on delay and Doppler shift estimation errors.

Fig. 2 plots the AF and the corresponding contour plot of the phase modulated stepped frequency waveform. The number of frequency tones $L = 8$. In Fig. 2, we consider quadrature phase shift keying (QPSK) modulation and set $M = 4$. We have given the plot for one random sequence of phases and this particular phase sequence will be used in all the plots for the phase modulated waveform in the remainder of this section. Whilst not shown here due to the page limitation, we have provided a few additional plots in [35] for comparison purposes. Compared to the AF of the classical linear stepped frequency waveform given in [35, Fig. 2], the broader structure of the AF is slightly changed due to the phase modulation. To be more specific, when there is no phase modulation, most of the volume under the AF is concentrated in a ridge located in the first and third quadrants. When phase modulation is introduced, although there still exists a ridge, the volume is slightly spread out. However, the AF around the origin is almost unaffected by the phase modulation.

To gain more insight into the AF and see the behaviour around the origin more clearly, Fig. 3 provides one dimensional cuts of the AFs in [35, Fig. 2] and Fig. 2. From Fig. 3 (a) we observe that the zero-Doppler cut is changed due to the phase modulation but the change of the highest side-lobe level as well as the curvature at the origin is negligible, which indicates that phase modulation has little impact on the delay estimation accuracy. From Fig. 3 (b) we

$$\mathrm{CRLB}_\tau \approx \frac{C^{-1}L^2T}{2LB\left(L-\sum_{l=0}^{L-2}\cos\left(\omega_l T+\theta_l-\theta_{l+1}\right)\right)-3T^3\left(\sum_{l=0}^{L-1}(2l+1)\omega_l\right)^2}, \tag{23}$$

$$\mathrm{CRLB}_\omega \approx \frac{24C^{-1}B\left(L-\sum_{l=0}^{L-2}\cos\left(\omega_l T+\theta_l-\theta_{l+1}\right)\right)}{2L^2T^2B\left(L-\sum_{l=0}^{L-2}\cos\left(\omega_l T+\theta_l-\theta_{l+1}\right)\right)-3LT^5\left(\sum_{l=0}^{L-1}(2l+1)\omega_l\right)^2}. \tag{24}$$

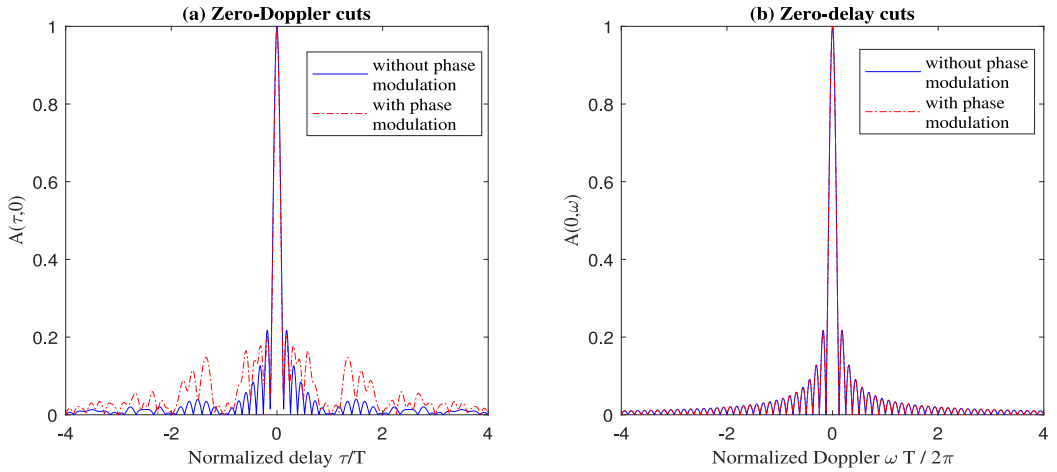

FIGURE 3. The (a) zero-Doppler cuts and (b) zero-delay cuts of the AFs in [35, Fig. 2] (blue solid line) and Fig. 2 (red dashed line). The AF cuts in [35, Fig. 2] are for a traditional linear stepped frequency radar waveform, i.e., without phase modulation.

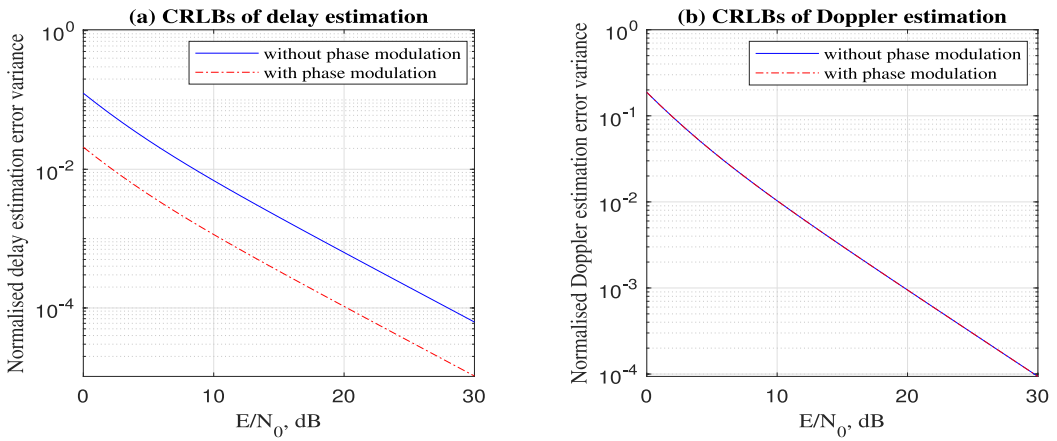

FIGURE 4. The (a) approximated CRLBs on delay estimation errors given in (25) and (27) and (b) approximated CRLBs on Doppler shift estimation errors given in (26) and (28) for stepped frequency based waveforms with and without phase modulation.

observe that the zero-delay cuts of the two AFs are exactly the same, which indicates that the phases of subpulses have no impact on the zero-delay cut. Hence, there is very little impact on the Doppler shift estimation accuracy. This also agrees with the theoretical results in (19) as well as the analysis in (26).

Next, we focus on quantitative performance measurements of the delay and Doppler shift estimation accuracy, which can be illustrated by the CRLBs. Fig. 4 (a) plots the normalised CRLBs on delay estimation error in (25) and (27) versus the received signal-to-noise ratio (SNR). Fig. 4 (b) plots the normalised CRLBs on Doppler shift estimation error in (26) and (28) versus the received SNR. We focus on the waveform considered in Fig. 2 and compare the performance against the waveform without phase modulation. As is illustrated in Fig. 4 (a), the CRLB on delay estimation error decreases by changing the phases of subpulses. The approximated CRLB for the un-modulated stepped frequency waveform in (27) is maximised since $f_0 = 0$ Hz and $\Delta f = 1/T$ Hz, thus any phase change will result in a lower delay CRLB, as is shown by (25). Agreeing with (26), the CRLB on Doppler estimation error remains unchanged with phase modulation, as is illustrated in Fig. 4 (b).

IV. FREQUENCY PERMUTATIONS AND PHASE SHIFT KEYING BASED WAVEFORMS

In this section, we introduce a novel frequency modulation on top of the phase modulation introduced in Section III to embed more data into the waveform in (1). In the linear stepped frequency radar waveform in (11), the frequency was linearly changed according to (2). Motivated by [31], we proceed to change the order of frequency tones on top of the phase modulation, such that the randomisation in the frequency tones can be used to send more data. Interestingly, we observe that random permutation of the frequency tones results in a reasonably small AF side-lobe level on average and has limited impact on the radar local accuracy.

A. INCORPORATING FREQUENCY PERMUTATIONS

Consider the sequence of L frequency tones $f_0, f_1, \ldots, f_{L-1}$ illustrated by (2). If a single frequency tone is used only

once in a particular waveform having L subpulses, we can formulate $L!$ of these waveforms. The frequencies of the i-th waveform, $\{f_0^i, \ldots, f_{L-1}^i\}$, follow the i-th permutation from a total of $L!$ permutation sequences where f_l^i denotes the frequency in the l-th slot of the i-th waveform. The i-th waveform can be expressed as

$$s_i(t) = \sqrt{\frac{E}{LT}} \sum_{l=0}^{L-1} s_p(t - lT) \exp\left(j\left(2\pi f_l^i (t - lT)\right)\right). \quad (29)$$

To increase the achievable data rate, we introduce phase modulation which is performed independently of the frequency modulation. Note that we change the phase in a discrete manner from subpulse to subpulse, as discussed in Section III, allowing us to independently change the phase and frequency of each subpulse. If M-ary phase shift keying is used, we can formulate $L! \times M^L$ possible waveforms in total. The i-th waveform can be expressed as

$$s_i(t) = \sqrt{\frac{E}{LT}} \sum_{l=0}^{L-1} s_p(t - lT) \exp\left(j\left(2\pi f_l^i (t - lT) + \theta_l^i\right)\right), \quad (30)$$

where $\theta_l^i \in \{0, 2\pi/M, \ldots, 2\pi(M-1)/M\}$ denotes the phase of the l-th subpulse of the i-th waveform and the frequencies of the i-th waveform follow one of the $L!$ permutations given by

$$\begin{aligned} \Psi_1 = \cdots = \Psi_{M^L} &= \{f_0, \ldots, f_{L-2}, f_{L-1}\} \\ \Psi_{M^L+1} = \cdots = \Psi_{2M^L} &= \{f_0, \ldots, f_{L-1}, f_{L-2}\} \\ &\vdots \\ \Psi_{(L!-1)\times M^L+1} = \cdots = \Psi_{L!\times M^L} &= \{f_{L-1}, \ldots, f_1, f_0\}. \end{aligned} \quad (31)$$

For simplicity, we define $M_T = L! \times M^L$ to be the total number of possible waveforms.

While combining phase modulation with frequency permutation increases the number of waveforms, not all degrees of freedom (DoFs) are used in transmitting communications symbols when using the proposed modulation scheme in (30) because of the restriction on the frequency sequence. If we relax the restriction on using permutations and allow frequencies to repeat, we obtain L-ary frequency shift keying (FSK) but not frequency permutations. Combining the L-ary FSK with the M-ary PSK, the total number of waveforms is $(LM)^L$, while our proposed scheme has $L! \times M^L$ waveforms, resulting in a loss in the maximum data rate of $\log_2(L^L/L!)/LT$. However, we should note that using all the DoFs can result in unstable radar performance. More specifically, FSK based waveforms do not have deterministic control of the occupied bandwidth. In addition, the structure of the AF depends significantly on the selection of particular frequency sequences. In extreme cases, some sequences can deliver poor performance both in terms of the main-lobe width and peak side-lobe level.

B. GENERATION OF THE WAVEFORMS

As has been discussed, we can formulate M_T possible waveforms under the novel modulation scheme in Section IV-A. When L and M are large, a huge look-up table is required to map the data to the waveform. However, we can avoid the use of the look-up table by implementing the mapping using the *Lehmer code* [36]. This was initially proposed in [31] for the frequency permutation based waveforms but could be easily adapted for the case with both frequency and phase modulation. To be more specific, if the incoming data symbol is represented as an index i where $i \in \{1, \ldots, M_T\}$, the integer $(\lfloor \frac{i-1}{M^L} \rfloor + 1)$ is mapped to a particular permutation of L frequency tones using a factorial number system where $\lfloor \cdot \rfloor$ denotes the operation of rounding the argument down. Then, the integer $(i - 1 - \lfloor \frac{i-1}{M^L} \rfloor M^L)$ is converted to a sequence of L digits with base number M and sent into a standard M PSK modulator to generate a particular sequence of L phases.

C. AMBIGUITY FUNCTION

In order to derive the AF, we normalise the signal energy to one and re-express the i-th waveform in (30) as

$$s_i(t) = \sqrt{\frac{1}{LT}} \sum_{l=0}^{L-1} s_p(t - lT) \exp\left(j\left(\omega_l^i (t - lT) + \theta_l^i\right)\right), \quad (32)$$

where $\omega_l^i = 2\pi f_l^i$ is the frequency in radians per second. Following similar steps as in Section III-A, we can write the complex AF of the waveform in (32) as

$$\begin{aligned} \hat{A}(\tau, \omega) = \frac{1}{LT} \sum_{l=0}^{L-1} \sum_{n=0}^{L-1} \hat{A}_p\left(\tau + (n-l)T, \omega - \left(\omega_n^i - \omega_l^i\right)\right) \\ \times e^{j\left(\omega lT + \omega_n^i (\tau + (n-l)T) + \left(\theta_l^i - \theta_n^i\right)\right)}. \end{aligned} \quad (33)$$

Taking the absolute value of (33), we express the AF of the waveform as

$$\begin{aligned} A(\tau, \omega) = \left| \frac{1}{LT} \sum_{l=0}^{L-1} \sum_{n=0}^{L-1} \hat{A}_p\left(\tau + (n-l)T, \omega - \left(\omega_n^i - \omega_l^i\right)\right) \right. \\ \left. \times e^{j\left(\omega lT + \omega_n^i (\tau + (n-l)T) + \left(\theta_l^i - \theta_n^i\right)\right)} \right|. \end{aligned} \quad (34)$$

Similarly, the zero-Doppler cut and the zero-delay cut can be expressed as

$$\begin{aligned} A(\tau, 0) = \left| \frac{1}{LT} \sum_{l=0}^{L-1} \sum_{n=0}^{L-1} \hat{A}_p\left(\tau + (n-l)T, \omega_l^i - \omega_n^i\right) \right. \\ \left. \times e^{j\left(\omega_n^i (\tau - (n-l)T) + \left(\theta_l^i - \theta_n^i\right)\right)} \right|, \end{aligned} \quad (35)$$

$$\begin{aligned} A(0, \omega) = \left| \frac{1}{LT} \sum_{l=0}^{L-1} \sum_{n=0}^{L-1} \hat{A}_p\left((n-l)T, \omega - \left(\omega_n^i - \omega_l^i\right)\right) \right. \\ \left. \times e^{j\left(\omega lT + \omega_n^i (n-l)T + \left(\theta_l^i - \theta_n^i\right)\right)} \right|. \end{aligned} \quad (36)$$

The zero-delay cut in (36) can be simplified as

$$A(0,\omega)=\left|\frac{1}{LT}\sum_{l=0}^{L-1}\hat{A}_p(0,\omega)e^{j\omega lT}\right|, \tag{37}$$

which implies that the zero-delay cut is not affected by frequency permutation and phase change.

As is analysed in [31], the overall structure of the AF resulting from the random stepped frequency permutation based waveform has a narrow main-lobe and small sidelobes. In Section IV-E, using numerical examples we demonstrate that these desirable radar properties are little affected. Such an AF can achieve good radar performance since low side-lobe levels can reduce the probability for the radar receiver to pick a wrong delay Doppler cell. More specifically, when a noisy reflected signal is passed through the radar receiver, the probability that the noisy matched filter output at the delay and Doppler shift values corresponding to a high AF side-lobe exceeds that corresponding to the AF main-lobe is significant. This leads to an incorrect detection, i.e., picking the wrong point on the delay Doppler plane, while low AF side-lobes can reduce the probability of incorrect detection.

Low AF side-lobe levels are also important for clutter [31]. Generally speaking, there is a useful averaging effect on the AF side-lobes because the transmitter sends waveforms based on random incoming information, which we do not control. This indicates that clutter enters via the average AF side-lobe level, averaged over different waveforms. Therefore, in the following we analyse the overall performance using the average of the AF. We note from (33) that the complex AF in (33) is a sum of bounded and weakly correlated complex exponential terms whose exponents are random variables. The weak correlation between terms is due to the independent and identically distributed (i.i.d) phase terms in the exponents. In this situation, the modified central limit theory such as [37] motivates the use of a Gaussian approximation to the distribution of the complex AF value when the number of terms in the summation is large. More specifically, $\hat{A}(\tau,\omega)$ can be approximated by a complex Gaussian random variable whose real and imaginary parts are independent. Thus, $A(\tau,\omega)$ can be approximated using a Rician distribution which can be fully described using the mean of $\hat{A}(\tau,\omega)$ and the second moment of $A(\tau,\omega)$. Following the steps in Appendix A, the second moment of the AF in (34) can be expressed as

$$E\left[A^2(\tau,\omega)\right]=\begin{cases}a_0(T), & -T\le\tau<0,\\ a_0(-T), & 0\le\tau<T,\\ a_1, & \text{otherwise},\end{cases} \tag{38}$$

where $a_0(\cdot)$ and a_1 are defined in (39) and (40), shown at the bottom of the page, respectively, and

$$b(x)=\begin{cases}L, & x\in\mathbb{Z},\\ \frac{1-\exp(j2\pi xL)}{1-\exp(j2\pi x)}, & \text{otherwise}.\end{cases} \tag{41}$$

The mean of the complex Gaussian random variable is the mean of the complex AF, which can be expressed as

$$E\left[\hat{A}(\tau,\omega)\right]=\begin{cases}\frac{\hat{A}_p(\tau,\omega)e^{j\omega_0\tau}b(\Delta f\tau)b(\omega T/(2\pi))}{L^2T}, & |\tau|<T,\\ 0, & \text{otherwise}.\end{cases} \tag{42}$$

Detailed steps of the derivation of (42) are provided in Appendix B. Using (38), (42) and the Rician approximation, the mean of $A(\tau,\omega)$ can be expressed as

$$E[A(\tau,\omega)]\approx\sqrt{\frac{\pi}{2}}\sigma(\tau,\omega)L_{1/2}\left(-\frac{\left|E\left[\hat{A}(\tau,\omega)\right]\right|^2}{2\sigma^2(\tau,\omega)}\right), \tag{43}$$

where $\sigma(\tau,\omega)$ denotes the standard deviation of the real and imaginary parts of the approximation, which can be expressed as

$$\sigma(\tau,\omega)=\sqrt{\frac{E\left[A^2(\tau,\omega)\right]-\left|E\left[\hat{A}(\tau,\omega)\right]\right|^2}{2}}, \tag{44}$$

and $L_{1/2}(x)$ is a Laguerre function which is defined as

$$L_{1/2}(x)=e^{x/2}\left[(1-x)I_0\left(-\frac{x}{2}\right)-xI_1\left(-\frac{x}{2}\right)\right], \tag{45}$$

$$\begin{aligned}a_0(x)=&\frac{(\tau+x)^2}{L^3(L-1)T^2}\mathrm{sinc}^2\left(\frac{\omega}{2\pi}(\tau-T)\right)\left(|b(\Delta f\tau)|^2-L\right)\left(\left|b\left(\frac{\omega T}{2\pi}\right)\right|^2-L\right)\\&+\frac{1}{L^3T^2}\sum_{\substack{k=-(L-1)\\k\neq0}}^{L-1}(L-|k|)\tau^2\mathrm{sinc}^2\left(\left(\frac{\omega}{2\pi}-k\Delta f\right)\tau\right)+\frac{(\tau+x)^2}{LT^2}\mathrm{sinc}^2\left(\frac{\omega}{2\pi}(\tau+x)\right),\end{aligned} \tag{39}$$

$$\begin{aligned}a_1=&\frac{1}{L^3(L-1)T^2}\sum_{\substack{k=-(L-1)\\k\neq0}}^{L-1}(L-|k|)\left\{\left(L-\left|\lfloor\frac{\tau}{T}\rfloor\right|\right)\left(T-\tau+\lfloor\frac{\tau}{T}\rfloor T\right)^2\right.\\&\times\mathrm{sinc}^2\left(\left(\frac{\omega}{2\pi}-k\Delta f\right)\left(T-\tau+\lfloor\frac{\tau}{T}\rfloor T\right)\right)\\&\left.+\left(L-\left|\lfloor\frac{\tau}{T}\rfloor+1\right|\right)\left(\tau-\lfloor\frac{\tau}{T}\rfloor T\right)^2\mathrm{sinc}^2\left(\left(\frac{\omega}{2\pi}-k\Delta f\right)\left(\tau-\lfloor\frac{\tau}{T}\rfloor T\right)\right)\right\}.\end{aligned} \tag{40}$$

with $I_0(x)$ and $I_1(x)$ the modified Bessel functions [38].

We note from (42) that $E[\hat{A}(\tau,\omega)]$ is zero when $|\tau| \geq T$. Therefore, (43) can be simplified by considering a Rayleigh approximation, resulting in

$$E[A(\tau,\omega)] \approx \frac{\sqrt{\pi E\left[A^2(\tau,\omega)\right]}}{2}, \quad |\tau| \geq T. \tag{46}$$

We also observe from (44) that $\sigma(0,\omega) = 0$, which indicates that the variance of the approximation is 0 when $\tau = 0$. This is consistent with (37) that the zero-delay cut of the AF is invariant with the selection of waveforms. By substituting τ with 0 in (43) and using the asymptotic expansions of $I_1(x)$ and $I_2(x)$ when $x \to \infty$ [38], we can express $E[A(0,\omega)]$ as

$$E[A(0,\omega)] = \left|E\left[\hat{A}(0,\omega)\right]\right|, \tag{47}$$

which is exactly the same as the invariant zero-delay cut in (37). Thus, the approximation in (43) is an exact result when $\tau = 0$.

Please note that the approximation in (43) is accurate when the number of terms in the summation is large. We note that this condition does not hold for all (τ,ω) pairs. When $\tau = kT$ and $\omega = r\Delta f$, where both k and r are integers, the complex AF can be derived using (34) as

$$\hat{A}(kT, r\Delta f) = \frac{1}{j2\pi\,\Delta f LT}\sum_{l=k}^{L-1}\left\{e^{j\left(\theta_l^i-\theta_{l-k}^i\right)} \times \frac{e^{j2\pi\,\Delta f\left(n_l^i-n_{l-k}^i+r\right)T}-1}{r+n_l^i-n_{l-k}^i}e^{j2\pi rl}\right\}. \tag{48}$$

Note that the number of terms in (48) is small. This indicates that the approximation is inaccurate when $\tau = kT$ and $\omega = r\Delta f$ or close to these regions. However, the approximation in (43) is still reasonable on the majority of the delay-Doppler plane.

In Section III-C, we further discuss the performance of the AFs and the approximations with different parameters using numerical examples.

D. FISHER INFORMATION MATRIX AND CRAMER-RAO LOWER BOUNDS

In this section, we follow similar steps as in Section and derive the FIM for the new waveform. Replacing ω_m and θ_m in (20) to (22) with ω_m^i and θ_m^i, respectively, the new FIM elements can be expressed as

$$J_{11} \approx \frac{2CB}{LT}\left(L-\sum_{l=0}^{L-2}\cos\left(\omega_0 T+\theta_l^i-\theta_{l+1}^i\right)\right), \tag{49}$$

$$J_{12} = J_{21} \approx -\frac{CT^2}{2}\sum_{l=0}^{L-1}\omega_l^i(2l+1), \tag{50}$$

$$J_{22} = \frac{CL^2T^2}{12}. \tag{51}$$

Based on (49)-(51), the CRLBs of the delay estimation and Doppler shift estimation errors can be approximated by (52) and (53), respectively. Based on [33, eq. (10.94), (10.95)], (52) and (53) can be further simplified to looser bounds, which can be expressed as

$$\mathrm{CRLB}_\tau \approx \frac{C^{-1}LT}{2B\left(L-\sum_{l=0}^{L-2}\cos\left(\omega_0 T+\theta_l^i-\theta_{l+1}^i\right)\right)}, \tag{54}$$

$$\mathrm{CRLB}_\omega \approx \frac{12C^{-1}}{L^2T^2}. \tag{55}$$

Again, the simplified expressions in (54) and (55) clearly show the effect of parameters on the estimation errors. The delay estimation error lower bound in (54) is inversely proportional to B and to the effective bandwidth, $1/T$, of a single subpulse. The Doppler shift estimation error lower bound in (55) is inversely proportional to the square of time duration of the whole waveform LT. Compared to (27) and (28), the frequency permutation has no effect on both CRLB_τ and CRLB_ω. In addition, compared to [31, eq. (48), (49)], it can be found that the phase modulation has exactly no effect on the simplified CRLB_ω while it does affect CRLB_τ. Similar to Section III-B, the maximum value (when all $\cos(\cdot)$ terms equal 1) and minimum value (when all $\cos(\cdot)$ terms equal -1) of CRLB_τ in (55) are kept unchanged when phase modulation is introduced. The analysis is supported by the numerical examples in Section III-C.

E. NUMERICAL EXAMPLES

In this section, we provide numerical examples to verify the theoretical analyses in Section III-A and Section IV-D. Fig. 5 and Fig. 6 illustrate the AFs and the corresponding contour plots for the random frequency permutation based waveforms for $L = 8$ with and without phase modulation, respectively The phase sequence of the waveform in Fig. 6 is the same as that in Fig. 2 and the frequency permutation is randomly

$$\mathrm{CRLB}_\tau \approx \frac{C^{-1}L^2T}{2LB\left(L-\sum_{l=0}^{L-2}\cos\left(\omega_0 T+\theta_l^i-\theta_{l+1}^i\right)\right)-3T^3\left(\sum_{l=0}^{L-1}(2l+1)\omega_l^i\right)^2}, \tag{52}$$

$$\mathrm{CRLB}_\omega \approx \frac{24C^{-1}B\left(L-\sum_{l=0}^{L-2}\cos\left(\omega_0 T+\theta_l^i-\theta_{l+1}^i\right)\right)}{2L^2T^2B\left(L-\sum_{l=0}^{L-2}\cos\left(\omega_0 T+\theta_l^i-\theta_{l+1}^i\right)\right)-3LT^5\left(\sum_{l=0}^{L-1}(2l+1)\omega_l^i\right)^2}. \tag{53}$$

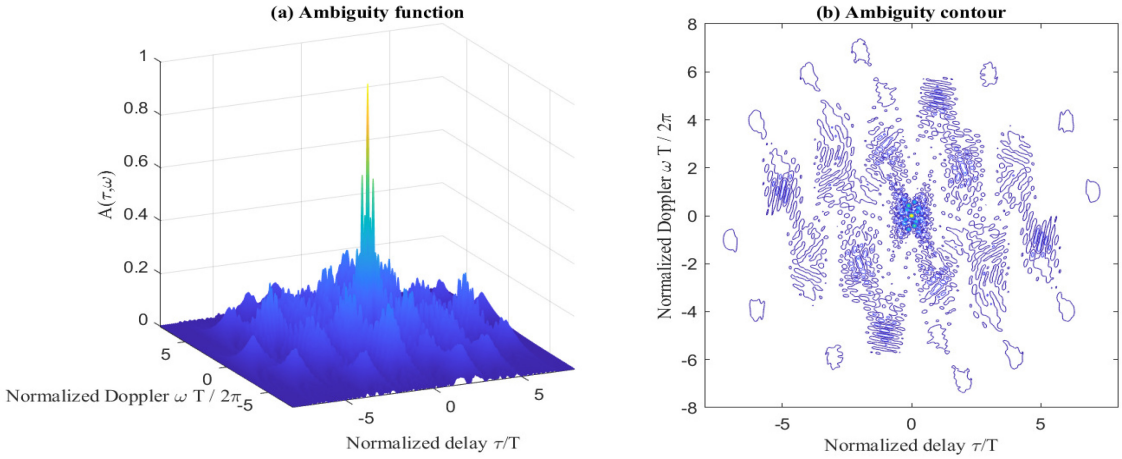

FIGURE 5. AF of a frequency permutation based waveform for $L = 8$ and $\Delta f = 1/T$. The frequency sequence is $[f_2, f_7, f_5, f_0, f_4, f_1, f_6, f_3]$.

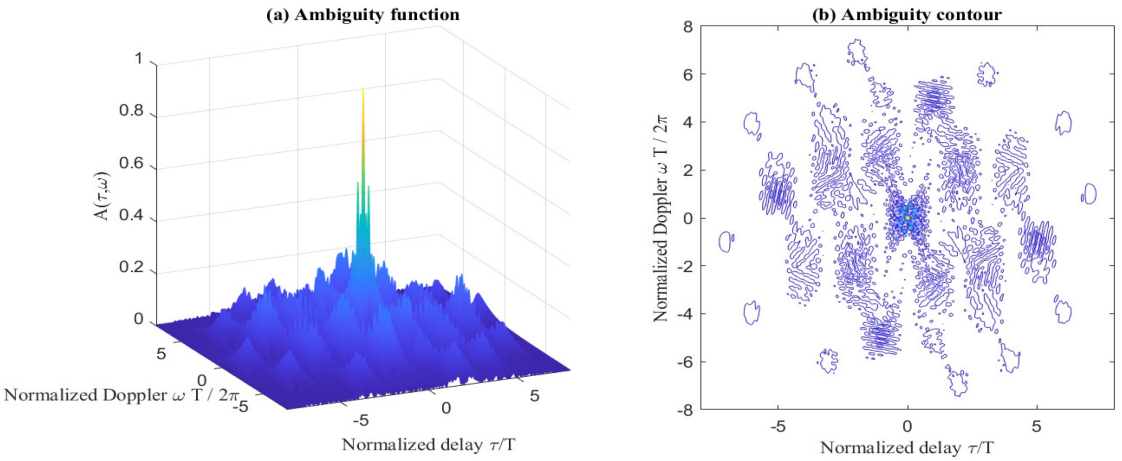

FIGURE 6. The AF of a frequency permutation and PSK based waveform for $L = 8$, $M = 4$ and $\Delta f = 1/T$. The frequency sequence is $[f_2, f_7, f_5, f_0, f_4, f_1, f_6, f_3]$. The phase sequence is $[3\pi/4, 3\pi/4, 3\pi/4, \pi/2, 3\pi/4, \pi/2, \pi/4, \pi/2]$.

generated. Both of them will be fixed in the AF and CRLB examples for the remainder of this section. We observe that the main-lobes of the AFs in Fig. 5 and Fig. 6 are very similar, which again implies that the phase modulation has negligible impact on the AF around the origin. In addition, by comparing Fig. 5 with [35, Fig. 2] and Fig. 6 with Fig. 2, it can be observed that the frequency permutation has a larger impact on the broader structure of the AF than the phase modulation. By randomly choosing a frequency permutation, the volume under the AF is more likely to be evenly spread over the delay-Doppler plane as is evident by the side-lobe structure of Fig. 5 and Fig. 6 compared to that of a waveform with an ascending frequency sequence given in [35, Fig. 2] and Fig. 2.

Fig. 7 plots the one dimensional cuts of the AFs in Fig. 5 and Fig. 6. The zero-Doppler cuts in Fig. 7 (a) indicate that the change due to the phase modulation in both the highest side-lobe level and the curvature at the origin is negligible. As is discussed in Section III-A, the zero-delay cut is not affected by the phase modulation, which can also be observed in Fig. 7 (b). Compared to Fig. 3, we also notice that the frequency permutation does not affect the zero-delay cuts. This agrees with the expression in (37) as well as the analysis in (55).

Fig. 6 and Fig. 7 illustrate the side-lobe levels using an example AF. In order to analyse the average side-lobe performance of the AFs of all possible waveforms, Fig. 8 plots the empirical mean of the AFs and the average AF based on the Rician approximation in (43) with $L = 8$ and $M = 4$. We observe from the empirical mean in Fig. 8 (a) and (b) that the side-lobe level of the AFs is low on average. By comparing Fig. 8 (c) and (d) with (a) and (b), we observe that the Rician approximation has a similar structure to the empirical mean, and that the approximation is accurate in general.

Fig. 9 further studies the accuracy of the approximation by plotting the difference between the Rician approximation mean and the empirical mean of the AFs in Fig. 8. We observe that the error is insignificant on the majority of the delay-Doppler plane, except when τ and ω are close to

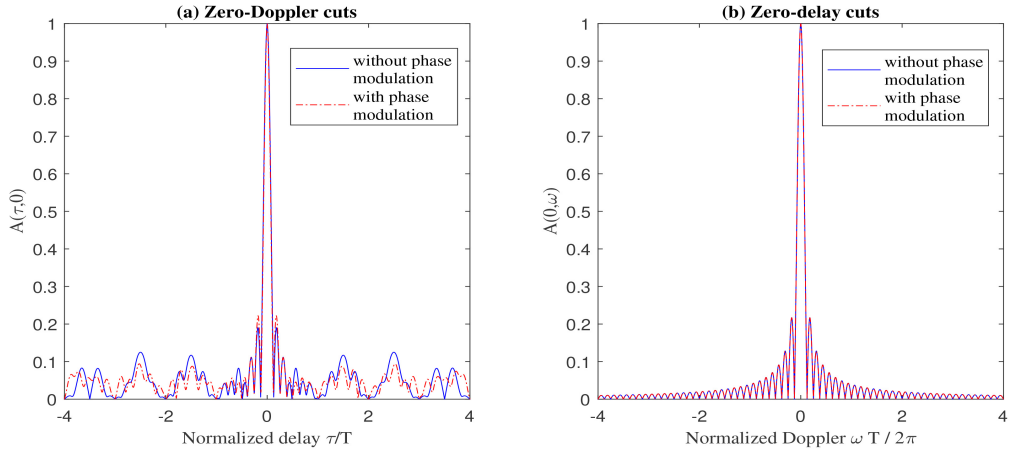

FIGURE 7. The (a) zero-Doppler cuts and (b) zero-delay cuts of the AFs in Fig. 5 and Fig. 6.

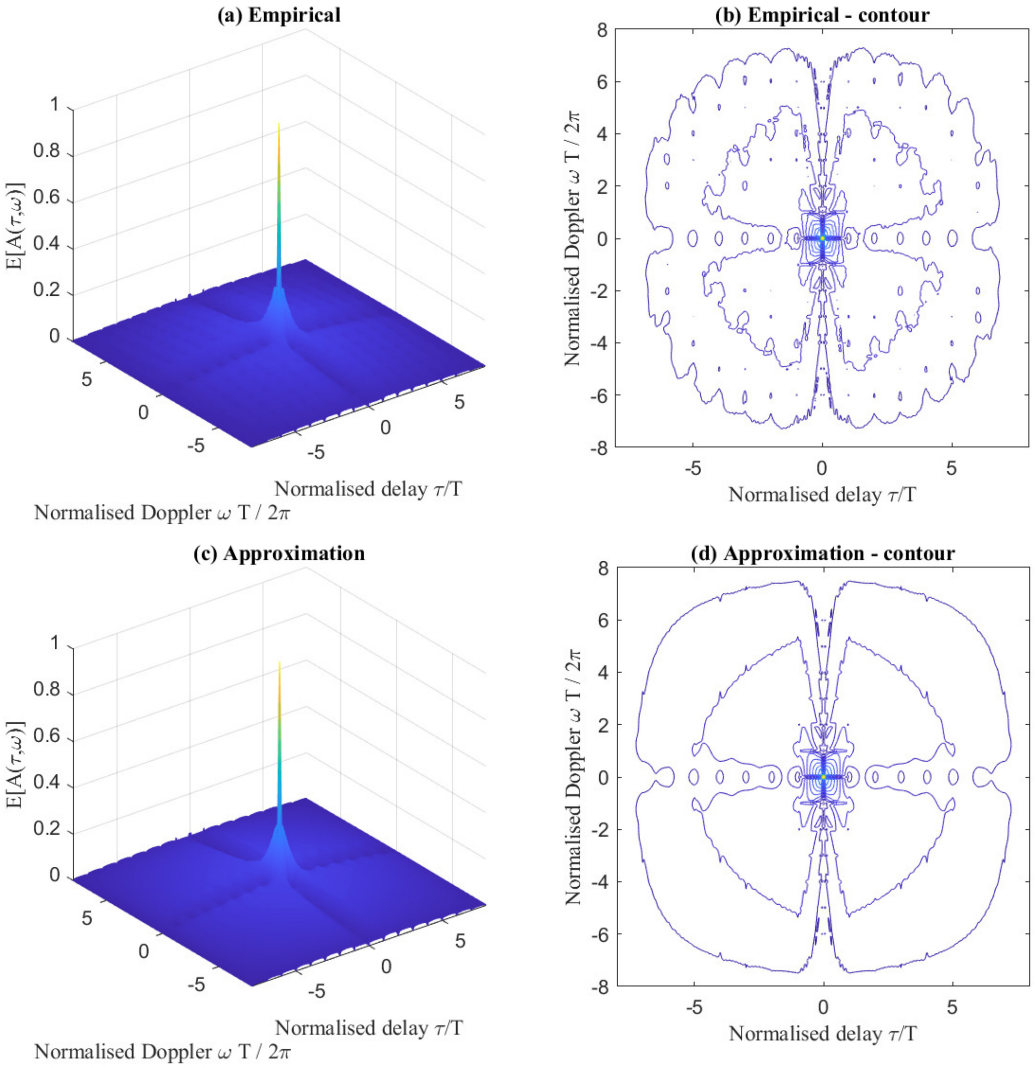

FIGURE 8. (a) The empirical mean of the AFs (b) its corresponding contour plot and (c) the average AF based on the Rician approximation (d) its corresponding contour plot for $L = 8$, $M = 4$ and $\Delta f = 1/T$.

integer multiples of T and $2\pi\Delta f$, respectively. In order to analyse the significance of the error, we evaluate the values of the empirical mean and the difference on the diagonal of the delay-Doppler plane, i.e., when $\tau = kT, \omega = 2\pi \times k\Delta f$, $k \in \{1, \ldots, L-1\}$. The difference decreases slowly from 0.0209 to 0.0127 with k while the mean AF decrease rapidly

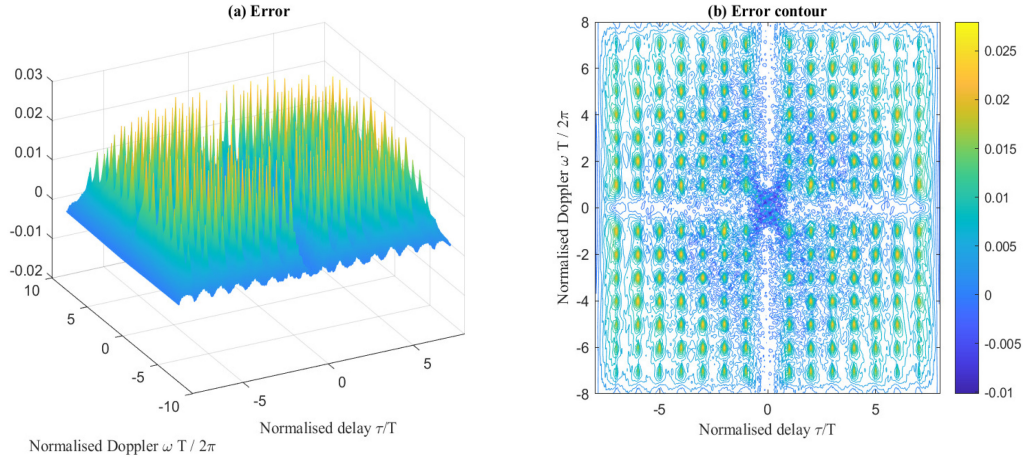

FIGURE 9. The (a) difference between the Rician approximation mean and the empirical mean of the AFs in Fig. 8 and (b) its contour plot.

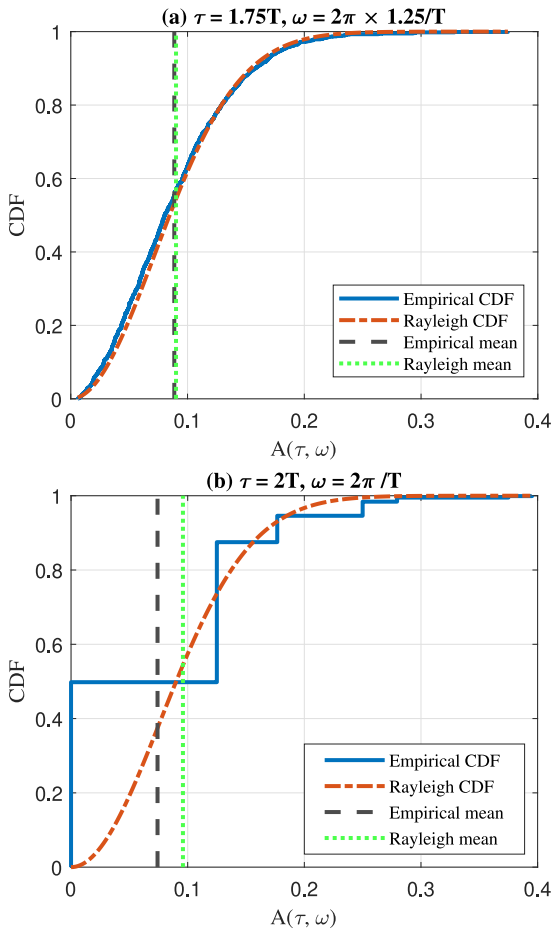

FIGURE 10. The empirical CDFs and the Rayleigh approximations of (a) $A(\tau = 1.75T, \omega = 2\pi \times 1.25/T)$ and (b) $A(\tau = 2T, \omega = 2\pi \times /T)$ with $L = 8$, $M = 4$ and $\Delta f = 1/T$.

from 0.0828 to 0.0021, which indicates that the significance of the error increases when moving away from the origin. However, this is acceptable since the high side-lobe levels close to the origin are of more interest. Furthermore, we observe from Fig. 9 that the Rician approximation becomes higher than the empirical mean when τ and ω are close to integer multiples of T and $2\pi\Delta f$ except for the area around the origin. Hence, the method is conservative and provides a reliable indication of low AF side-lobe levels.

Fig. 10 plots the empirical cumulative distribution functions (CDFs) of $A(\tau, \omega)$ for $L = 8$ and $M = 4$ and the corresponding approximations for two examples of τ, ω values. Note that the simple Rayleigh approximation in (46) is used as both τ values are greater than T. We observe in Fig. 10 (b) that when τ is an integer multiple of T and ω is an integer multiple of $2\pi\Delta f$, the empirical distribution is "discrete" since the number of complex exponentials in the summation in (48) is small. However, away form these points we see an excellent fit, as can be observed in Fig. 10 (a).

In order to analyse the impact of phase modulation on the mean of the AFs, Fig. 11 compares the zero-Doppler cuts and zero-delay cuts of the average AFs in Fig. 8 and the empirical average of the AFs of waveforms without phase modulation. We observe that the approximation in (43) shows high accuracy on the two axes. We also observe that the difference between the AF cuts with and without phase modulation is insignificant, which indicates that the phase modulation has a limited impact on the average side-lobe levels in the two AF cuts.

Fig. 12 plots the CDF and empirical probability density function (PDF) of the normalised peak side-lobe levels of the AFs with and without phase modulation for $L = 8$ and $M = 4$. When phase modulation is introduced, both the CDF and PDF become smoother. Besides, from Fig. 12 (b), we observe that the empirical mean of the peak side-lobe level is slightly decreased from 0.326 to 0.303 with phase modulation. This clearly illustrates that phase modulation does not have a significant effect on the average side-lobe levels of the AFs.

Fig. 13 plots the normalised CRLBs on delay estimation error in [31, eq. (48)] and (54), as well as the normalised

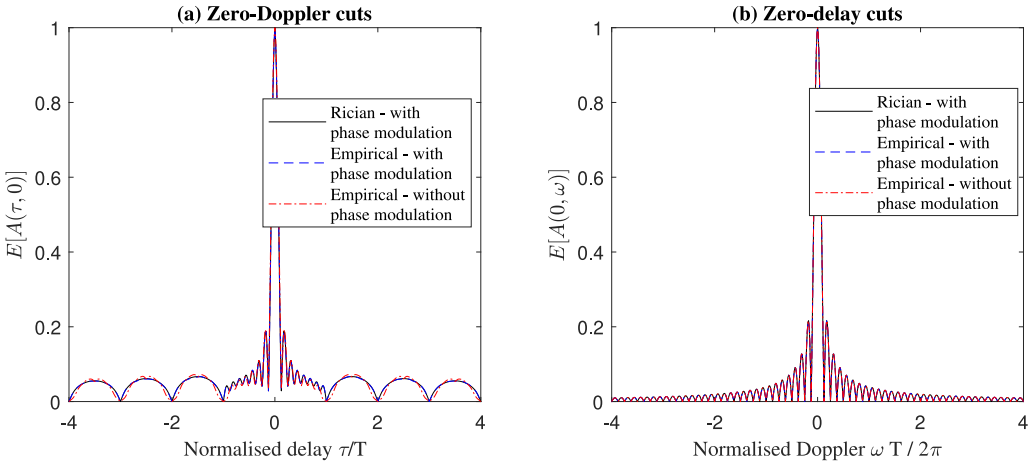

FIGURE 11. The (a) zero-Doppler cuts and (b) zero-delay cuts of the average AFs in Fig. 8 and the empirical average of the AFs of waveforms without phase modulation.

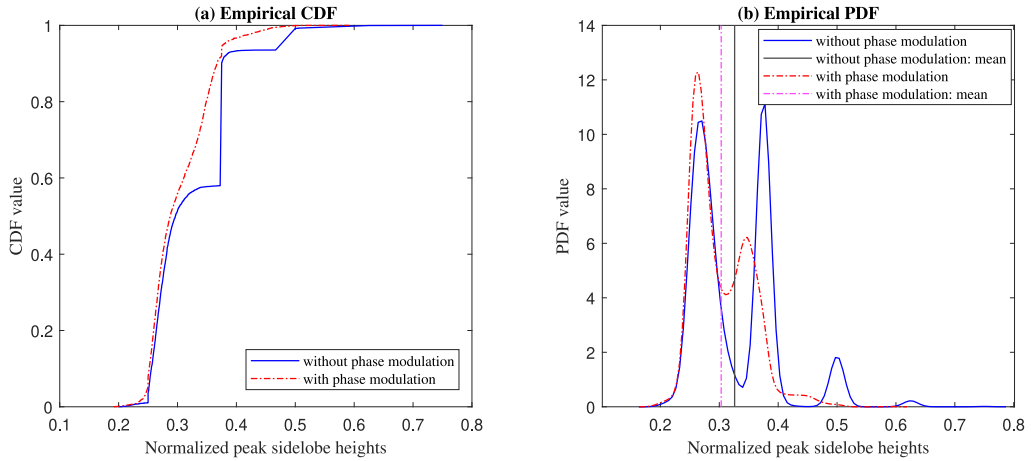

FIGURE 12. The (a) empirical CDF and (b) empirical PDF of the normalised peak side-lobe levels of AFs with and without phase modulation for $L = 8$ and $M = 4$.

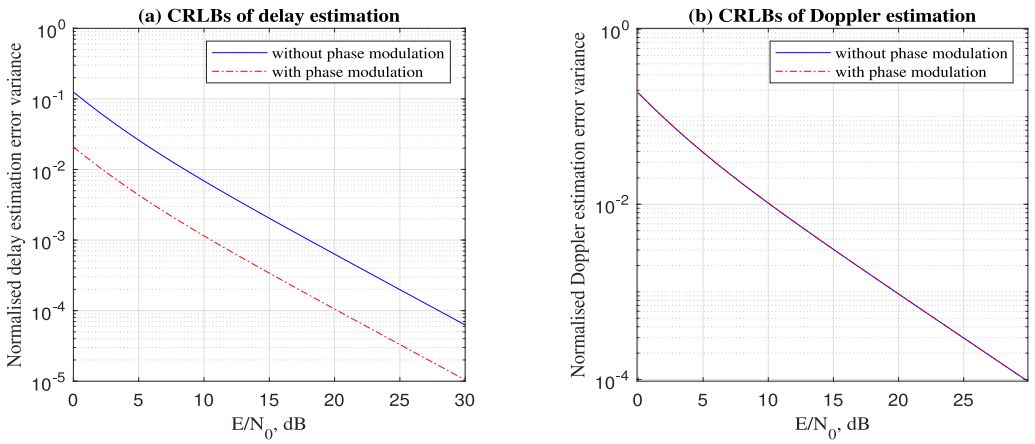

FIGURE 13. The (a) approximated CRLBs in (54) on delay estimation errors and (b) approximated CRLBs in (55) on Doppler shift estimation errors for stepped frequency based waveforms with and without phase modulation.

CRLBs on Doppler shift estimation error in [31, eq. (49)] and (55) versus the received SNR, respectively. Since $f_0 = 0$ Hz and $\Delta f = 1/T$ Hz, the simplified CRLB_τ in (54) is maximised without phase modulation and is decreased due to the change of phases, which is shown in Fig. 13 (a). Agreeing with the analytical results, the simplified CRLB_ω in (55) remains unchanged with phase change, as is shown in Fig. 13 (b).

V. COMMUNICATIONS PERFORMANCE ANALYSIS

In this section, we focus on the communication performance of the proposed waveform. In Section III, we consider the traditional MPSK modulation for which the communication performance is quite well known and therefore is not discussed in this paper. In Section IV we consider combining MPSK modulation with frequency permutation, which results in a new signalling scheme. In this section, we focus on this interesting new communication system and analyse its performance in terms of the block error probability. We perform the optimal ML detection at the communication receiver and derive analytical expressions for the union bound, nearest neighbour approximation and a new upper bound on the block error probability. In addition, we propose the implementation of an efficient communication receiver based on the Hungarian algorithm. While we only focus on the block error probability performance, we should notice that the achievable data rate of the proposed waveform depends on the total number of waveforms we can generate which is $\lfloor \log_2(M_T) \rfloor / LT$ bits/second.

A. MAXIMUM LIKELIHOOD DETECTION

Assume there are N antennas at the communications receiver. The baseband received signal at time t can be represented by an $N \times 1$ vector

$$\boldsymbol{r}_c(t) = \boldsymbol{h} s_i(t) + \boldsymbol{n}(t), \tag{56}$$

where $\boldsymbol{h}$ is the fading channel vector, $s_i(t)$ is the transmitted signal and $\boldsymbol{n}(t)$ is an AWGN vector in which the power spectral density (PSD) of each element is N_0. The transmission of $s_i(t)$ is assumed to be equally likely among all M_T possible waveforms. Suppose the channel vector is known at the receiver, then ML detection of the received signal is given by

$$\hat{s}_i(t) = argmax_{s_k(t) \in \{s_1(t), \ldots, s_{M_T}(t)\}} \Re\left\{ \int_0^{LT} s_k^*(t) \boldsymbol{h}^H \boldsymbol{r}_c(t) dt \right\}, \tag{57}$$

where $\Re\{\cdot\}$ denotes the operation of taking the real part of the argument.

B. ERROR PROBABILITY ANALYSIS

1) AWGN CHANNEL

First, let us consider the simple AWGN channel model. By assuming a unit channel gain, the fading vector satisfies $\boldsymbol{h}^H \boldsymbol{h} = N$. If the i-th waveform, $s_i(t)$, is transmitted the probability of the correct detection of the waveform is given by

$$P_c(i) = \Pr\left[\xi_{ii} = \max_{k \in \{1, \ldots, M_T\}} \xi_{ik} \right], \tag{58}$$

where ξ_{ik} is the k-th decision variable when $s_i(t)$ is transmitted, and is given by

$$\xi_{ik} = \Re\left\{ \int_0^{LT} s_k^*(t) \boldsymbol{h}^H \boldsymbol{r}_c(t) dt \right\}. \tag{59}$$

Since the transmission of each waveform is assumed to be equally likely, the average probability of making a wrong detection is

$$P_e = \frac{1}{M_T} \sum_{i=1}^{M_T} (1 - P_c(i)). \tag{60}$$

We note that it is difficult to calculate the exact expression of P_e since it requires multi-dimensional integrals. Therefore, we consider the union bound on P_e, which is given by

$$P_e \leq P_e^{UB} = \frac{1}{M_T} \sum_{i=1}^{M_T} \sum_{\substack{k=1, \\ k \neq i}}^{M_T} P_{ik}, \tag{61}$$

where P_{ik} denotes the pairwise error probability (PEP) that the k-th signal is preferred over the i-th signal when the i-th signal is transmitted and is given by

$$P_{ik} = \Pr[\xi_{ik} - \xi_{ii} \geq 0]. \tag{62}$$

Since the distribution of the distances between a particular waveform $s_i(t)$ and all other waveforms is unchanged with the particular selection of index i, we can further simplify the union bound as

$$P_e^{UB} = \sum_{k=2}^{M_T} P_{1k}. \tag{63}$$

Similar to [31, eq. (10)-(11)], next we proceed to analyse P_{ik}, by substituting (59) into (62) and rearranging the expressions to obtain

$$P_{ik} = \Pr\left[\frac{E\left(L - \sum_{q=1}^{L-d} \cos\left(\theta_{l(q)}^k - \theta_{l(q)}^i\right)\right)}{L} \boldsymbol{h}^H \boldsymbol{h} < Z_1 \right], \tag{64}$$

where d is the number of frequency tones $s_i(t)$ and $s_k(t)$ differ by, $l(q)$ is the index of the q-th subpulse where $s_i(t)$ and $s_k(t)$ have the same frequency and $Z_1 = \Re\{\boldsymbol{h}^H \int_0^{LT} (s_k^*(t) - s_i^*(t)) \boldsymbol{n}(t) dt\}$. When conditioned on the channel fading, Z_1 is a Gaussian random variable with zero mean and variance $E(L - \sum_{q=1}^{L-d} \cos(\theta_{l(q)}^k - \theta_{l(q)}^i)) N_0 \boldsymbol{h}^H \boldsymbol{h} / L$. Thus we can express the PEP in (62) as

$$P_{ik} = \Pr\left[\sqrt{\boldsymbol{h}^H \boldsymbol{h}} \leq \alpha_{ik} Z \right], \tag{65}$$

where

$$\alpha_{ik} = \sqrt{\frac{LN_0}{E\left(L - \sum_{q=1}^{L-d} \cos\left(\theta_{l(q)}^k - \theta_{l(q)}^i\right)\right)}},$$

and $Z \sim \mathcal{N}(0, 1)$ is a standard Gaussian random variable. By setting $\boldsymbol{h}^H \boldsymbol{h} = N$, the pairwise error probability P_{ik} over the AWGN channel can be represented as

$$P_{ik} = Q\left(\frac{\sqrt{N}}{\alpha_{ik}} \right), \tag{66}$$

where $Q(\cdot)$ is the Gaussian Q-function. Substituting (66) to (63) we find the resulting union bound over the AWGN channel as

$$P_e^{UB} = \sum_{k=2}^{M_T} Q\left(\frac{\sqrt{N}}{\alpha_{1k}}\right). \tag{67}$$

We note that, if L and M are large, there are $M_T - 1$ pairwise error probabilities to be added up, which will make the union bound far above the exact error probability, especially in the low SNR region. To provide a better approximation, we derive the nearest neighbour approximation of the error probability, in which we only consider the pairwise error probabilities corresponding to the nearest neighbours [39]. When $M > 2$, the nearest neighbours of a particular waveform $s_i(t)$ are the waveforms with the same frequency permutation as $s_i(t)$, while the phase is only different in a single subpulse by the amount of $2\pi/M$. The number of nearest neighbours for a particular waveform is $2L$. Thus the nearest neighbour approximation can be expressed as

$$P_e^{NN} = 2LP_{1k}^{NN}, \tag{68}$$

where P_{1k}^{NN} is the PEP that the nearest neighbour $s_k(t)$ is preferred over $s_1(t)$ when $s_1(t)$ is transmitted, which can be expressed as

$$P_{1k}^{NN} = Q\left(\frac{\sqrt{N}}{\alpha_{ik}^{NN}}\right), \tag{69}$$

where

$$\alpha_{ik}^{NN} = \sqrt{\frac{LN_0}{E\left(1-\cos\left(\frac{2\pi}{M}\right)\right)}}. \tag{70}$$

When $M = 2$, however, the set of nearest neighbours of a particular waveform $s_i(t)$ is the union of two subsets. The first subset has a size of L, which contains the waveforms with the same frequency permutation as $s_i(t)$, while the phase is only different in a single subpulse by the amount of π. In the second subset, the waveforms have $L-2$ subpulses in the same positions as $s_i(t)$. For the other two subpulses, the order of the frequency tones is different compared to $s_i(t)$ while phases do not matter. The size of the second subset is $2L(L-1)$. Therefore, when $M = 2$, the nearest neighbour approximation can be expressed as

$$P_e^{NN} = \left(2L^2 - L\right)P_{1k}^{NN}, \tag{71}$$

where P_{1k}^{NN} in (71) can be expressed by (69) with $\alpha_{ik}^{NN} = \sqrt{\frac{LN_0}{2E}}$. Thus, the nearest neighbour approximation over the AWGN channel can be written as

$$P_e^{NN} = \begin{cases} 2LQ\left(\sqrt{\frac{NE(1-\cos(2\pi/M))}{LN_0}}\right), & M > 2 \\ (2L^2-L)Q\left(\sqrt{\frac{2NE}{LN_0}}\right), & M = 2. \end{cases} \tag{72}$$

2) CORRELATED FADING CHANNELS

Under fading channels, we first focus on the correlated Rician fading channel with a line-of-sight (LOS) path and a scattered path. For such a system, the channel fading vector can be expressed as

$$\boldsymbol{h} = \sqrt{\frac{K}{K+1}}\Delta + \sqrt{\frac{1}{K+1}}\boldsymbol{R}_u^{1/2}\boldsymbol{u}, \tag{73}$$

where Δ denotes the $N \times 1$ complex LOS phase vector with the i-th element having the property $|\Delta_i|^2 = 1$, $\boldsymbol{u} \sim \mathcal{CN}(0, \boldsymbol{I}_N)$, K is the Rician factor which denotes the relative strength of the LOS path to the scattered path and $\boldsymbol{R}_u$ denotes the $N \times N$ correlation matrix of the scattered component. As $\boldsymbol{R}_u$ is a symmetric matrix it can be expressed as

$$\boldsymbol{R}_u = \boldsymbol{V}\boldsymbol{\Omega}\boldsymbol{V}^H, \tag{74}$$

where $\boldsymbol{V}$ is unitary and $\boldsymbol{\Omega} = \text{diag}(\lambda_1, \ldots, \lambda_N)$ is a diagonal matrix containing the eigenvalues $\lambda_1, \ldots, \lambda_N$ of $\boldsymbol{R}_u$. We denote the j-th element of the vector $(\boldsymbol{V}^H\Delta)$ as $(\boldsymbol{V}^H\Delta)_j$. Whilst not given here due to page limitations, after lengthy mathematical manipulations, P_{1k} for correlated Rician channels can be derived as

$$P_{1k} = \frac{1}{\pi}\int_0^{\pi/2}\prod_{j=1}^{N}\left(\frac{2(K+1)\alpha_{1k}^2\sin^2\theta}{\lambda_j + 2(K+1)\alpha_{1k}^2\sin^2\theta}\right) \times \exp\left(-K\sum_{j=1}^{N}\frac{|(\boldsymbol{V}^H\Delta)_j|^2}{\lambda_j + 2(K+1)\alpha_{1k}^2\sin^2\theta}\right)d\theta. \tag{75}$$

The full derivation of (75) is included in the arXiv version [35, Appendix A]. Substituting (75) into (63), (68) and (71), we obtain the union bound as well as the nearest neighbour approximation of the error probability over a correlated Rician fading channel.

Note that for the special case of Rayleigh fading channels where the fading vector $\boldsymbol{h}$ does not have the LOS component, the pairwise error probability can be simplified to

$$P_{1k} = \frac{1}{\pi}\int_0^{\pi/2}\prod_{j=1}^{N}\left(\frac{2\alpha_{1k}^2\sin^2\theta}{\lambda_j + 2\alpha_{1k}^2\sin^2\theta}\right)d\theta. \tag{76}$$

3) TIGHTER UPPER BOUND

As has been stated in Section V-B1, when L and M are large, the union bound can be very loose, especially in the low SNR regime. This problem becomes more severe in fading channels since the channels are random vectors. Therefore, in the following we propose a tighter upper bound on the error probability for fading channels as

$$P_e \le P_e^{NB} = \min_{\gamma \ge 0}\left\{\Pr\left[\boldsymbol{h}^H\boldsymbol{h} < \gamma\right] + \Pr\left[\boldsymbol{h}^H\boldsymbol{h} \ge \gamma\right]\sum_{k=2}^{M_T}\tilde{P}_{1k}\right\}, \tag{77}$$

where γ is a threshold defined for the total channel gain and

$$\tilde{P}_{1k} = \Pr\Big[\xi_{11} < \xi_{1k} \mid \boldsymbol{h}^H\boldsymbol{h} \geq \gamma\Big]. \tag{78}$$

In (77), the bound is created by assuming that a detection error always occurs when the channel gain is lower than a defined threshold γ. The minimisation with respect to γ in (77) is taken to make the upper bound as tight as possible. Using the result in (65) and following the steps in [35, Appendix B], (78) can be expressed as

$$\tilde{P}_{1k} = \frac{1}{\pi \Pr\big[\boldsymbol{h}^H\boldsymbol{h} \geq \gamma\big]} \int_{\gamma}^{\infty} \int_{0}^{\pi/2} f_{\boldsymbol{h}^H\boldsymbol{h}}(x) \times \exp\left(-\frac{x}{2\alpha_{1k}^2 \sin^2\theta}\right) d\theta\, dx, \tag{79}$$

where $f_{\boldsymbol{h}^H\boldsymbol{h}}(x)$ is the PDF of $\boldsymbol{h}^H\boldsymbol{h}$.

For the correlated Rayleigh fading channel, we can rewrite $\boldsymbol{h}^H\boldsymbol{h}$ as

$$\boldsymbol{h}^H\boldsymbol{h} = \boldsymbol{u}^H\boldsymbol{R}_u\boldsymbol{u} \equiv \sum_{j=1}^{N} \lambda_j |\boldsymbol{u}_j|^2, \tag{80}$$

where $\boldsymbol{u}_j$ is the j-th element of the vector $\boldsymbol{u}$ and $\equiv$ indicates statistical equivalence. Thus, the PDF of the random variable in (80) can be expressed as [40]

$$f^{\text{Ray}}_{\boldsymbol{h}^H\boldsymbol{h}}(x) = \begin{cases} \sum_{j=1}^{N} \frac{b_j}{\lambda_j} e^{-x/\lambda_j}, & x \geq 0 \\ 0, & x < 0, \end{cases} \tag{81}$$

where $b_j = \lambda_j^{N-1} \prod_{\substack{n=1 \\ n\neq j}}^{N} 1/(\lambda_j - \lambda_n)$. Substituting (81) into (79) and (77), we can express the new upper bound over the correlated Rayleigh fading channel as

$$P_e^{NB} = \min_{\gamma \geq 0} \left\{ \sum_{j=1}^{N} b_j \left(1 - e^{-\frac{x}{\lambda_j}}\right) + \frac{1}{\pi} \sum_{k=2}^{M_T} \sum_{j=1}^{N} \frac{2 b_j \alpha_{1k} \sin^2\theta}{\lambda_j + 2\alpha_{1k}\sin^2\theta} \times \int_0^{\pi/2} \exp\left(-\gamma\left(\frac{1}{2\alpha_{1k}\sin^2\theta} + \frac{1}{\lambda_j}\right)\right) d\theta \right\}. \tag{82}$$

Under the numerical examples in Section V-D we illustrate the accuracy of the new bound and highlight that it is much tighter than the union bound when L and M are large.

C. OPTIMAL COMMUNICATIONS RECEIVER

In this section we propose the implementation of an efficient communications receiver for the novel signalling scheme presented in Section IV. The optimal receiver based on the ML detection rule in (57) looks for the maximum output over the correlations between the received signal and all possible transmitted signals. If an exhaustive search is applied to find the maximum, the receiver has a worst case complexity of $\mathcal{O}(M_T)$, which means the detection process will be prohibitively slow when L and M are large. Instead of correlating the whole received signal with the reference signals as in (57), an efficient receiver can be implemented using the correlation in each subpulse

$$x_{\bar{m},l} = \Re\left\{ \int_{(l-1)T}^{lT} \boldsymbol{h}^H \boldsymbol{r}_c(t) \phi_{\bar{m}}(t - (l-1)T) dt \right\}, \tag{83}$$

to formulate the matrix

$$\boldsymbol{X} = \left(x_{\bar{m},l}\right) \in \mathbb{R}^{(ML)\times L}. \tag{84}$$

The basis function $\phi_{\bar{m}}(t)$ is defined as

$$\phi_{\bar{m}}(t) = s_p(t) \exp(j(2\pi f_{n-1} t + \theta_m)),$$

where $\bar{m} \in \{1, 2, \ldots, ML\}$ is the row index of the $(\bar{m}, l)$-th element in $\boldsymbol{X}$, $l \in \{1, 2, \ldots, L\}$ is the column index of the $(\bar{m}, l)$-th element in $\boldsymbol{X}$ which denotes the index of the subpulse, $n = (\lfloor \frac{\bar{m}-1}{M} \rfloor + 1) \in \{1, 2, \ldots, L\}$ denotes the index of the frequency of the basis function $\phi_{\bar{m}}(t)$, $m = (\bar{m} - \lfloor \frac{\bar{m}-1}{M} \rfloor M) \in \{1, 2, \ldots, M\}$ and $\theta_m = 2\pi(m-1)/M$ is the phase of $\phi_{\bar{m}}(t)$.

Then, we split $\boldsymbol{X}$ into L^2 blocks of M elements whose basis functions have the same frequency and time slot. Using the maximum element in each block, we can formulate a new matrix, which can be expressed as

$$\boldsymbol{Y} = \left(y_{n,l}\right) \in \mathbb{R}^{L\times L}, \tag{85}$$

where

$$y_{n,l} = \max_{\bar{m} \in \{M(n-1)+1, \ldots, Mn\}} x_{\bar{m},l}. \tag{86}$$

The row indices of $y_{n,l}$ in the original matrix $\boldsymbol{X}$ is stored separately in $\bar{m}_{n,l}$. Note that the basis function used for $y_{n,l}$ is a complex exponential with frequency f_{n-1}. The worst case complexity of finding L^2 maximums in L^2 blocks is $\mathcal{O}(L^2 \times M)$ if an exhaustive search is used.

To detect the frequency of each subpulse, we apply the Hungarian algorithm to $\boldsymbol{Y}$ to select L elements $\hat{r}_l$, $l \in \{1, \ldots, L\}$, such that these elements are in L different rows and L different columns, and the sum of the L elements is maximised. The detection of the frequency $\hat{f}^i_{l-1}$ is determined by the row index $\hat{n}_l$ of the selected element in the l-th column. Note that the Hungarian algorithm has a worst case time complexity of $\mathcal{O}(L^3)$ [41].

To detect the phase of each subpulse, we use the recorded indices $\bar{m}_{n,l}$ of the L elements selected by the Hungarian method. The detection of the phase $\hat{\theta}^i_{l-1}$ is determined by the row index of the selected element in the l-th column of the original matrix $\boldsymbol{X}$.

Algorithm 1 summarises the main steps of the Hungarian algorithm based communication receiver. The proposed optimal receiver is an efficient implementation of the optimal ML detector.

D. NUMERICAL EXAMPLES

In this section we provide numerical examples to support the theoretical analysis of the communication performance in Section V-B. Fig. 14 to 16 illustrate the error probability of the waveform over different communication channel models.

Algorithm 1 Modified Hungarian Algorithm for Optimal Communications Receiver

Formulate $\boldsymbol{X} = \left(x_{\bar{m},l}\right) \in \mathbb{R}^{(ML)\times L}$ using (83) and (84)
for $l = 1$ to L **do**
  for $n = 1$ to L **do**
    $y_{n,l} \leftarrow \max_{\bar{m}\in\{M(n-1)+1,\ldots,Mn\}} x_{\bar{m},l}$
    $\bar{m}_{n,l} \leftarrow argmax_{\bar{m}\in\{M(n-1)+1,\ldots,Mn\}} x_{\bar{m},l}$
  end for
end for
$\boldsymbol{Y} \leftarrow (y_{n,l}) \in \mathbb{R}^{L\times L}$
Apply the Hungarian algorithm to matrix $\boldsymbol{Y}$ following the steps in [31, algorithm 1] to get L elements $\hat{r}_l$ and their row indices $\hat{n}_l$, where $l \in \{1, \ldots, L\}$
for $l = 1$ to L **do**
  Detection of the frequency of the l-th subpulse $\hat{f}^i_{l-1} \leftarrow f_{\hat{n}_l-1}$
  Detection of the phase of the l-th subpulse $\hat{\theta}^i_{l-1} \leftarrow \frac{2\pi\lfloor(\bar{m}_{\hat{n}_l,l}-1)/M\rfloor}{M}$
end for

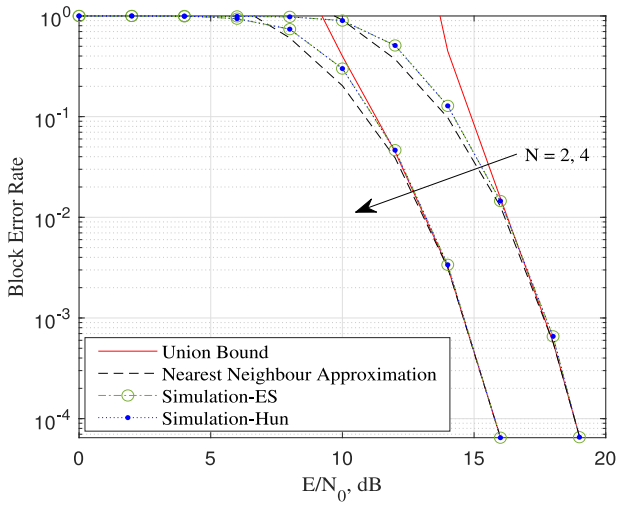

FIGURE 14. The block error rate versus average received SNR for $L = 8$, $M = 4$ and $N = 2, 4$. The results are for the proposed baseband signalling model in an AWGN channel.

We mainly focus on the performance of the bounds and approximations derived in Section V-B.

Note that the analysis for correlated fading channels in Section V-B2 holds for all $\boldsymbol{R}_u$ but in this section we use the simple exponential correlation model. Hence, given a correlation coefficient $\rho \in [0, 1]$, the (i, j)-th entry of $\boldsymbol{R}_u$ can be written as

$$\boldsymbol{R}_u(i, j) = \rho^{|i-j|}. \tag{87}$$

Fig. 14 shows the block error rate versus the average received SNR in an AWGN channel with different numbers of receiver antennas, $N = 2, 4$. The parameters of the waveform are kept to be $L = 8$ and $M = 4$. As expected, the block error rate decreases with an increase in N due to the receive diversity gain. The union bounds generated using (67) always stay above the corresponding simulation results and approach the simulation curves in the high SNR region. Compared to the union bounds, the nearest neighbour approximations generated using (72) provide better approximations to the simulation results, especially in the low SNR region.

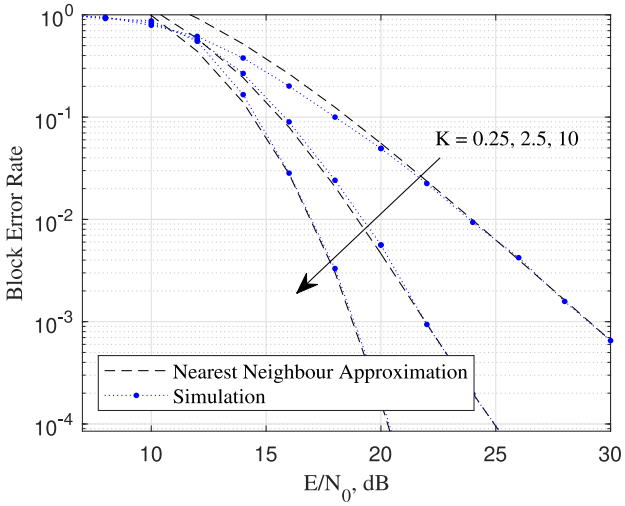

FIGURE 15. The block error rate versus average received SNR for $L = 8$, $M = 4$ and $N = 2$. The results are for the proposed baseband signalling model in correlated Rician fading channels with $K = 0.25, 2.5, 10$ and $\rho = 0.5$.

In order to verify the optimality of the efficient receiver, we plot the error probability performance of the Hungarian algorithm based receiver and the exhaustive search based receiver, denoted as "Simulation-Hun" and "Simulation-ES", respectively. Given the same received signal, the outputs of the two receivers are exactly the same, which results in the same error performance. For the convenience of simulation, we only provide error probability results from the Hungarian algorithm based receiver in the following figures.

Fig. 15 plots the block error rate versus the average received SNR in correlated Rician fading channels with different channel factors, $K = 0.25, 2.5, 10$. We set the waveform parameters, the number of receiving antennas and the correlation coefficient to be $L = 8$, $M = 4$, $N = 2$ and $\rho = 0.5$, respectively. As has been discussed, in fading channels the union bounds are very loose. Thus, we only show the nearest neighbour approximations using (71) with the PEP and α^{NN}_{1k} provided in (75) and (70), respectively. The block error rate decreases with K, since the LOS component is increased. The nearest neighbour approximations accurately approximate the corresponding simulation results in the high SNR region. However, the approximations become looser for smaller K in the low SNR region.

Fig. 16 plots the block error rate versus the average received SNR in a correlated Rayleigh fading channel with different numbers of receiver antennas, $N = 2, 4$. We set the waveform parameters and the correlation coefficient to be $L = 8$, $M = 4$ and $\rho = 0.5$, respectively. Similar to what we observe in Fig. 14, the block error rate decreases with an increase in N. Also, the nearest neighbour approach calculated using (68) and (71) approximates the simulation results more accurately with increasing N, especially in the low SNR region. The new upper bound in (82) is a tighter

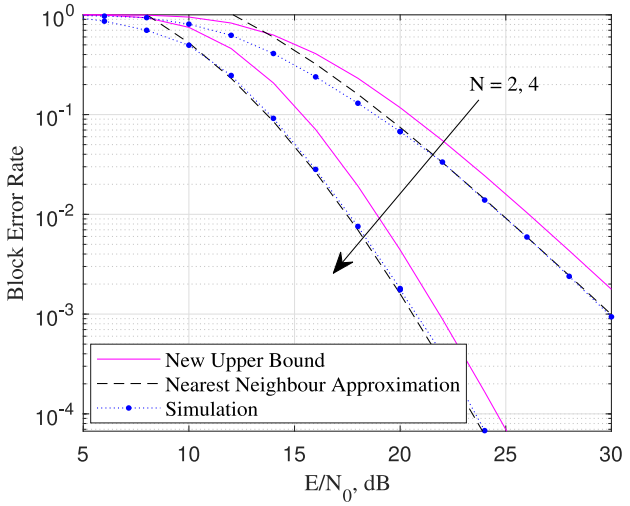

FIGURE 16. The block error rate versus average received SNR for $L = 8$, $M = 4$ and $N = 2, 4$. The results are for the proposed baseband signalling model in correlated Rayleigh fading channels with $\rho = 0.5$.

and more accurate performance bound on the block error rate compared to the union bound, which is not plotted in Fig. 16 since the value is always larger than 1. Therefore, for the proposed signalling scheme, the new upper bound does outperform the union bound over Rayleigh fading channels.

VI. CONCLUSION AND FUTURE EXTENSIONS

In this paper, we consider the integration of radar sensing and communications and propose a linear stepped frequency waveform and a frequency permutation based waveform, both with phase modulation. Compared to modulating data using phase only, the randomisation in frequency tones in the second signalling scheme allows more data to be transmitted.

Focusing on the fundamental theoretical aspects, we analyse the effect of phase and frequency modulation on the radar sensing functionality and establish an important and fundamental theoretical result which shows that the phase modulation has negligible effect on the radar local accuracy. More specifically, we derive the AFs of both waveforms to analyse the impact of phase change on local accuracy and side-lobe levels. To provide quantitative measurements of the impact of phase modulation on the local accuracy, we also derive approximations to the CRLBs on delay and Doppler estimation errors based on the FIMs. We conclude that the frequency permutations result in reasonably low AF side-lobe level in average and the phase modulation has little impact on the local estimation accuracy. From the perspective of communications, we focus on analysing the block error probability of the phase modulated frequency permutation based waveform. We consider the optimal ML detection and derive the union bound and the nearest neighbour approximation on the block error rate over AWGN channels and correlated Rician fading channels. We also propose a new tighter upper bound on the block error probability, for which a closed-form expression is derived under the case of Rayleigh fading channels.

Possible future extensions of this work includes the quantitative analysis of the effect of phase and frequency modulation on the side-lobe structure of the AF. From the communications perspective, it is desirable to extend the analysis to incorporate coding based on which a subset of possible waveforms can be selected to improve the error probability performance. On the other hand, using FSK instead of frequency permutations increases the number of waveforms and allows the use of more DoFs in data transmission. Nevertheless, the impact of FSK on radar performance requires further analysis.

APPENDIX A
THE SECOND MOMENT OF $|A(\tau,\omega)|$

For simplicity, we first re-write the expression of the AF in (34) as

$$A(\tau,\omega) = \left| \frac{1}{LT} \sum_{l=0}^{L-1} \sum_{n=0}^{L-1} a_{l,n} e^{j\left(\theta_l^i - \theta_n^i\right)} \right|, \tag{88}$$

where

$$a_{l,n} = \hat{A}_p\left(\tau + (n-l)T, \omega - \left(\omega_n^i - \omega_l^i\right)\right) e^{j\left(\omega l T + \omega_n^i(\tau + (n-l)T)\right)}. \tag{89}$$

By averaging over all possible frequency permutations and phase sequences, the second moment of $A(\tau,\omega)$ can be expressed as

$$E\left[A^2(\tau,\omega)\right] = \frac{1}{L^2T^2} \sum_{l=0}^{L-1}\sum_{n=0}^{L-1}\sum_{p=0}^{L-1}\sum_{q=0}^{L-1} E\left[a_{l,n} a_{pq}^* e^{j\left(\theta_l^i - \theta_n^i - \theta_p^i + \theta_q^i\right)}\right]. \tag{90}$$

Since frequencies and phases are independently modulated, we can re-write (90) as

$$E\left[A^2(\tau,\omega)\right] = \frac{1}{L^2T^2} \sum_{l=0}^{L-1}\sum_{n=0}^{L-1}\sum_{p=0}^{L-1}\sum_{q=0}^{L-1} E_{\Psi}\left[a_{l,n} a_{p,q}^*\right] T_{l,n,p,q}, \tag{91}$$

where Ψ denotes the frequency permutation and

$$T_{l,n,p,q} = E\left[e^{j\left(\theta_l^i - \theta_n^i - \theta_p^i + \theta_q^i\right)}\right]. \tag{92}$$

By noting the fact that $E_\theta[e^{jk\theta}] = 0$ when $k \in \mathbb{Z}\backslash\{0\}$, where $\mathbb{Z}$ denotes the set of all integers, we observe that $T_{l,n,p,q} = 1$ only when $(l = n, p = q, l \neq p)$, $(l = p, n = q,\ l \neq n)$ or $(l = n = p = q)$, otherwise $T_{l,n,p,q} = 0$. Therefore, (91) can be re-expressed as

$$E\left[A^2(\tau,\omega)\right] = \frac{1}{L^2T^2} E_{\Psi}\left[\sum_{\substack{l=0 \\ l\neq p}}^{L-1}\sum_{p=0}^{L-1} a_{l,l} a_{p,p}^* + \sum_{\substack{l=0 \\ l\neq n}}^{L-1}\sum_{p=0}^{L-1} |a_{l,n}|^2 + \sum_{l=0}^{L-1} |a_{l,l}|^2 \right]. \tag{93}$$

Substituting (89) into (91), the first term of the expectation can be expressed as

$$\sum_{\substack{l=0\\ l\neq p}}^{L-1}\sum_{p=0}^{L-1} E_{\boldsymbol{\Psi}}\left[a_{l,l}a_{p,p}^{*}\right] = \sum_{\substack{l=0\\ l\neq p}}^{L-1}\sum_{p=0}^{L-1}\left|\hat{A}_p(\tau,\omega)\right|^2 \times e^{j\omega(l-p)T} E_{\boldsymbol{\Psi}}\left[e^{j\left(\omega_l^i-\omega_p^i\right)\tau}\right]. \quad (94)$$

The frequency of subpulse l, ω_l^i, can be expressed as $2\pi(f_0 + k_l\Delta f)$, where k_l is uniformly distributed among $\{0, 1, \ldots, L-1\}$. Since only permutations of frequencies are considered, we observe that $k_l \neq k_p$. Thus the expectation on the right hand side of (94) can be further expressed as

$$E_{\boldsymbol{\Psi}}\left[e^{j\left(\omega_l^i-\omega_p^i\right)\tau}\right] = \frac{1}{L(L-1)}\sum_{\substack{k_l=0\\ k_l\neq k_p}}^{L-1}\sum_{k_p=0}^{L-1} e^{j2\pi(k_l-k_p)\Delta f\tau}. \quad (95)$$

After some straight forward mathematical manipulations, (94) can be expressed as

$$\sum_{\substack{l=0\\ l\neq p}}^{L-1}\sum_{p=0}^{L-1} E_{\boldsymbol{\Psi}}\left[a_{l,l}a_{p,p}^{*}\right] = \frac{1}{L(L-1)}\left|\hat{A}_p(\tau,\omega)\right|^2 \times \left(|b(\Delta f\tau)|^2 - L\right) \times \left(|b(\omega T/(2\pi))|^2 - L\right), \quad (96)$$

where $b(\cdot)$ is defined in (41). Substituting (89) into the second term and the third term of (93), $E[A^2(\tau,\omega)]$ can be expressed as (97), shown at the bottom of the page.

As is shown in (15), $\hat{A}_p(\tau,\omega) = 0$ when $|\tau| \geq T$. Thus, when $|\tau| \geq T$, it is obvious that the first and the third terms in (97) are zero and the second term is non-zero only if $l - n = \lfloor \tau/T \rfloor$ or $\lfloor \tau/T \rfloor + 1$. Therefore, $E[A^2(\tau,\omega)]$ for τ satisfying $\lfloor \tau/T \rfloor \geq 1$ or $\lfloor \tau/T \rfloor < -1$ can be expressed as in (98), shown at the bottom of the page.

We then focus on the derivation for $\lfloor \tau/T \rfloor \geq 1$ as the derivation for $\lfloor \tau/T \rfloor < -1$ is very similar. Using some straightforward mathematical manipulations, $E[A^2(\tau,\omega)]$ for τ satisfying $\lfloor \tau/T \rfloor \geq 1$ can be written as in (99), shown at the bottom of the page.

Because $(\omega^i_{l-\lfloor \tau/T \rfloor}, \omega^i_l)$ and $(\omega^i_{l-\lfloor \tau/T \rfloor - 1}, \omega^i_l)$ are two i.i.d pairs of frequencies, we denote $\Delta\omega \equiv \omega^i_{l-\lfloor \tau/T \rfloor} - \omega^i_l$. Note that $\Delta\omega$ is the difference of two random unequal frequencies and is independent to l. Thus, we further express $E[A^2(\tau,\omega)]$ as in (100), shown at the bottom of the page, where the expectation on the right hand side of (100) is taken with respect to $\Delta\omega$ whose probability mass function (pmf) is given by

$$p(\Delta\omega) = \frac{L-|k|}{L(L-1)}, \quad \Delta\omega = 2\pi k\Delta f, \quad k \in \{-(L-1), \ldots, -1, 1, \ldots, L-1\}. \quad (101)$$

Using the distribution of $\Delta\omega$, we can derive $E[A^2(\tau,\omega)]$ with some straightforward mathematical manipulations. The

$$E\left[A^2(\tau,\omega)\right] = \frac{1}{L^2T^2}\left(\frac{1}{L(L-1)}\left|\hat{A}_p(\tau,\omega)\right|^2\left(|b(\Delta f\tau)|^2 - L\right)\left(|b(\omega T/(2\pi))|^2 - L\right) + \sum_{\substack{l=0\\ l\neq n}}^{L-1}\sum_{p=0}^{L-1} E_{\boldsymbol{\Psi}}\left[\left|\hat{A}_p\left(\tau + (n-l)T, \omega - \left(\omega_n^i - \omega_l^i\right)\right)\right|^2\right] + \sum_{l=0}^{L-1} E_{\boldsymbol{\Psi}}\left[\left|\hat{A}_p(\tau,\omega)\right|^2\right]\right). \quad (97)$$

$$E\left[A^2(\tau,\omega)\right] = \frac{1}{L^2T^2}\left(\sum_{l=0}^{L-1}\sum_{n=l-\lfloor \tau/T \rfloor}^{L-1} E_{\boldsymbol{\Psi}}\left[\left|\hat{A}_p\left(\tau + (n-l)T, \omega - \left(\omega_n^i - \omega_l^i\right)\right)\right|^2\right] + \sum_{l=0}^{L-1}\sum_{n=l-\lfloor \tau/T \rfloor - 1}^{L-1} E_{\boldsymbol{\Psi}}\left[\left|\hat{A}_p\left(\tau + (n-l)T, \omega - \left(\omega_n^i - \omega_l^i\right)\right)\right|^2\right]\right), \quad \lfloor \tau/T \rfloor \geq 1 \text{ or } \lfloor \tau/T \rfloor < -1. \quad (98)$$

$$E\left[A^2(\tau,\omega)\right] = \frac{1}{L^2T^2}\left(\sum_{l=\lfloor \tau/T \rfloor}^{L-1} E_{\boldsymbol{\Psi}}\left[\left|\hat{A}_p\left(\tau - \lfloor\frac{\tau}{T}\rfloor T, \omega - \left(\omega^i_{l-\lfloor \tau/T \rfloor} - \omega_l^i\right)\right)\right|^2\right] + \sum_{l=\lfloor \tau/T \rfloor + 1}^{L-1} E_{\boldsymbol{\Psi}}\left[\left|\hat{A}_p\left(\tau - \left(\lfloor\frac{\tau}{T}\rfloor + 1\right)T, \omega - \left(\omega^i_{l-\lfloor \tau/T \rfloor - 1} - \omega_l^i\right)\right)\right|^2\right]\right), \quad \lfloor \tau/T \rfloor \geq 1. \quad (99)$$

$$E\left[A^2(\tau,\omega)\right] = (L - \lfloor \tau/T \rfloor)E_{\Delta\omega}\left[\hat{A}_p(\tau - \lfloor \tau/T \rfloor T, \omega - \Delta\omega)\right] + (L - \lfloor \tau/T \rfloor - 1)E_{\Delta\omega}\left[\hat{A}_p(\tau - (\lfloor \tau/T \rfloor + 1)T, \omega - \Delta\omega)\right], \quad \lfloor \tau/T \rfloor \geq 1. \quad (100)$$

resulting expression is given by

$$\begin{aligned}
&E\Big[A^2(\tau,\omega)\Big] \\
&= \frac{1}{L^3(L-1)T^2}\sum_{\substack{k=-(L-1)\\k\neq 0}}^{L-1}(L-|k|) \\
&\quad\times\Big\{\Big(L-\lfloor\frac{\tau}{T}\rfloor\Big)\Big(T-\tau+\lfloor\frac{\tau}{T}\rfloor T\Big)^2 \\
&\quad\times\operatorname{sinc}^2\Big(\Big(\frac{\omega}{2\pi}-k\Delta f\Big)\Big(T-\tau+\lfloor\frac{\tau}{T}\rfloor T\Big)\Big) \\
&\quad+\Big(L-\lfloor\frac{\tau}{T}\rfloor-1\Big)\Big(\tau-\lfloor\frac{\tau}{T}\rfloor T\Big)^2 \\
&\quad\times\operatorname{sinc}^2\Big(\Big(\frac{\omega}{2\pi}-k\Delta f\Big)\Big(\tau-\lfloor\frac{\tau}{T}\rfloor T\Big)\Big)\Big\}, \quad \lfloor\tau/T\rfloor\geq 1.
\end{aligned} \tag{102}$$

Similarly, $E[A^2(\tau,\omega)]$ for $\lfloor\tau/T\rfloor<-1$ can be expressed as

$$\begin{aligned}
&E\Big[A^2(\tau,\omega)\Big] \\
&= \frac{1}{L^3(L-1)T^2}\sum_{\substack{k=-(L-1)\\k\neq 0}}^{L-1}(L-|k|) \\
&\quad\times\Big\{\Big(L+\lfloor\frac{\tau}{T}\rfloor\Big)\Big(T-\tau+\lfloor\frac{\tau}{T}\rfloor T\Big)^2 \\
&\quad\times\operatorname{sinc}^2\Big(\Big(\frac{\omega}{2\pi}-k\Delta f\Big)\Big(T-\tau+\lfloor\frac{\tau}{T}\rfloor T\Big)\Big) \\
&\quad+\Big(L+\lfloor\frac{\tau}{T}\rfloor+1\Big)\Big(\tau-\lfloor\frac{\tau}{T}\rfloor T\Big)^2 \\
&\quad\times\operatorname{sinc}^2\Big(\Big(\frac{\omega}{2\pi}-k\Delta f\Big)\Big(\tau-\lfloor\frac{\tau}{T}\rfloor T\Big)\Big)\Big\}, \quad \lfloor\tau/T\rfloor<-1.
\end{aligned} \tag{103}$$

When $-1\geq\tau<1$, the first term and the third term in (97) are non-zero. They can be easily obtained by first calculating $|\hat{A}_p(\tau,\omega)|^2$ using (15)

$$\Big|\hat{A}_p(\tau,\omega)\Big|^2=\begin{cases}(\tau+T)^2\operatorname{sinc}^2\big(\frac{\omega}{2\pi}(\tau+T)\big), & -T\leq\tau<0,\\ (\tau-T)^2\operatorname{sinc}^2\big(\frac{\omega}{2\pi}(\tau-T)\big), & 0\leq\tau<T.\end{cases} \tag{104}$$

The second term in (97) can be derived following similar steps using the pmf of $\Delta\omega$ in (101).

APPENDIX B
THE MEAN OF $\hat{A}(\tau,\omega)$

Consider the complex AF of the frequency permutation and PSK based waveform in (33). We note that $\hat{A}_p(\tau,\omega)$ is non-zero only when $-T<\tau<T$. Thus, (33) can be further expressed as

$$\begin{aligned}
\hat{A}(\tau,\omega)=\frac{1}{LT}\sum_{l=0}^{L-1}\sum_{n=l-\lfloor\tau/T\rfloor-1}^{l-\lfloor\tau/T\rfloor}&e^{j(\omega lT+(\theta_l^i-\theta_n^i))}\\
&\times\hat{A}_p\Big(\tau+(n-l)T,\omega-\Big(\omega_n^i-\omega_l^i\Big)\Big)e^{j\omega_n^i(\tau+(n-l)T)}.
\end{aligned} \tag{105}$$

Since the phase modulation is independent of the frequency permutations, we write the mean of $\hat{A}(\tau,\omega)$ as

$$\begin{aligned}
E\Big[\hat{A}(\tau,\omega)\Big]=\frac{1}{LT}\sum_{l=0}^{L-1}\sum_{n=l-\lfloor\tau/T\rfloor-1}^{l-\lfloor\tau/T\rfloor}&e^{j\omega lT}E\Big[e^{j(\theta_l^i-\theta_n^i)}\Big]\\
&\times E\Big[\hat{A}_p(\tau+(n-l)T,\omega\\
&\quad-\Big(\omega_n^i-\omega_l^i\Big)\Big)e^{j\left(\omega_n^i(\tau+(n-l)T)\right)}\Big].
\end{aligned} \tag{106}$$

Since $E_\theta[e^{jk\theta}]=0$ when $k\in\mathbb{Z}\backslash\{0\}$, $E[e^{j(\theta_l^i-\theta_n^i)}]=0$ when $n\neq l$. Since $n\in\{l-\lfloor\tau/T\rfloor-1,l-\lfloor\tau/T\rfloor\}$, we can rewrite (106) as

$$E\Big[\hat{A}(\tau,\omega)\Big]=\begin{cases}\frac{\sum_{l=0}^{L-1}\hat{A}_p(\tau,\omega)E\Big[e^{j\omega_l^i\tau}\Big]e^{j\omega lT}}{LT}, & |\tau|<T,\\ 0, & \text{otherwise.}\end{cases} \tag{107}$$

By writing ω_l^i as $\omega_0+2\pi\Delta f\tau k_l^i$, $k_l^i=\{0,\ldots,L-1\}$, the mean of $e^{j\omega_l^i}$ can be expressed as

$$E\Big[e^{j\omega_l^i\tau}\Big]=\frac{e^{j\omega_0\tau}}{L}\sum_{k_l^i=0}^{L-1}e^{j2\pi\Delta f\tau k_l^i}. \tag{108}$$

Substituting (108) into (107) and using some straightforward mathematical manipulations, we express the mean of the complex AF as

$$E\Big[\hat{A}(\tau,\omega)\Big]=\begin{cases}\frac{\hat{A}_p(\tau,\omega)e^{j\omega_0\tau}b(\Delta f\tau)b(\omega T/(2\pi))}{L^2T}, & |\tau|<T,\\ 0, & \text{otherwise,}\end{cases} \tag{109}$$

where $b(\cdot)$ is defined in (41).

REFERENCES

[1] A. Hassanien, M. G. Amin, Y. D. Zhang, and F. Ahmad, "Signaling strategies for dual-function radar communications: An overview," *IEEE Aerosp. Electron. Syst. Mag.*, vol. 31, no. 10, pp. 36–45, Oct. 2016.

[2] C. Sturm and W. Wiesbeck, "Waveform design and signal processing aspects for fusion of wireless communications and radar sensing," *Proc. IEEE*, vol. 99, no. 7, pp. 1236–1259, Jul. 2011.

[3] L. Zheng and X. Wang, "Super-resolution delay-doppler estimation for OFDM passive radar," *IEEE Trans. Signal Process.*, vol. 65, no. 9, pp. 2197–2210, May 2017.

[4] F. Liu, C. Masouros, A. P. Petropulu, H. Griffiths, and L. Hanzo, "Joint radar and communication design: Applications, state-of-the-art, and the road ahead," *IEEE Trans. Commun.*, vol. 68, no. 6, pp. 3834–3862, Jun. 2020.

[5] J. A. Zhang et al., "An overview of signal processing techniques for joint communication and radar sensing," *IEEE J. Sel. Top. Signal Process.*, vol. 15, no. 6, pp. 1295–1315, Nov. 2021.

[6] A. Liu et al., "A survey on fundamental limits of integrated sensing and communication," *IEEE Commun. Surveys Tuts.*, vol. 24, no. 2, pp. 994–1034, 2nd Quart., 2022.

[7] P. Tan et al., "Integrated sensing and communication in 6G: Motivations, use cases, requirements, challenges and future directions," in *Proc. 1st IEEE Int. Online Symp. Joint Commun. Sens. (JC&S)*, 2021, pp. 1–6.

[8] F. Liu and C. Masouros, "A tutorial on joint radar and communication transmission for vehicular networks—Part I: Background and fundamentals," *IEEE Commun. Lett.*, vol. 25, no. 2, pp. 322–326, Feb. 2021.

[9] D. Ma, N. Shlezinger, T. Huang, Y. Liu, and Y. C. Eldar, "Joint radar-communication strategies for autonomous vehicles: Combining two key automotive technologies," *IEEE Signal. Process. Mag.*, vol. 37, no. 4, pp. 85–97, Jul. 2020.

[10] F. Liu and C. Masouros, "A tutorial on joint radar and communication transmission for vehicular networks—Part II: State of the art and challenges ahead," *IEEE Commun. Lett.*, vol. 25, no. 2, pp. 327–331, Feb. 2021.

[11] L. G. de Oliveira, B. Nuss, M. B. Alabd, A. Diewald, M. Pauli, and T. Zwick, "Joint radar-communication systems: Modulation schemes and system design," *IEEE Trans. Microw. Theory Techn.*, vol. 70, no. 3, pp. 1521–1551, Mar. 2022.

[12] R. Thoma, T. Dallmann, S. Jovanoska, P. Knott, and A. Schmeink, "Joint communication and radar sensing: An overview," in *Proc. 15th Eur. Conf. Antennas Prop. (EuCAP)*, 2021, pp. 1–5.

[13] S. D. Blunt, P. Yatham, and J. Stiles, "Intrapulse radar-embedded communications," *IEEE Trans. Aerosp. Electron. Syst.*, vol. 46, no. 3, pp. 1185–1200, Jul. 2010.

[14] P. M. McCormick, C. Sahin, S. D. Blunt, and J. G. Metcalf, "FMCW implementation of phase-attached radar-communications (PARC)," in *Proc. IEEE Radar Conf. (RadarConf)*, 2019, pp. 1–6.

[15] C. Sahin, J. Jakabosky, P. M. McCormick, J. G. Metcalf, and S. D. Blunt, "A novel approach for embedding communication symbols into physical radar waveforms," in *Proc. IEEE Radar Conf. (RadarConf)*, 2017, pp. 1498–1503.

[16] K. Wu, J. A. Zhang, X. Huang, and Y. J. Guo, "Frequency-hopping MIMO radar-based communications: An overview," *IEEE Aerosp. Electron. Syst. Mag.*, vol. 37, no. 4, pp. 42–54, Apr. 2022.

[17] W. Baxter, E. Aboutanios, and A. Hassanien, "Joint radar and communications for frequency-hopped MIMO systems," *IEEE Trans. Signal Process.*, vol. 70, pp. 729–742, 2022.

[18] K. Wu, J. A. Zhang, X. Huang, Y. J. Guo, and J. Yuan, "Reliable frequency-hopping MIMO radar-based communications with multi-antenna receiver," *IEEE Trans. Commun.*, vol. 69, no. 8, pp. 5502–5513, Aug. 2021.

[19] I. P. Eedara, A. Hassanien, M. G. Amin, and B. D. Rigling, "Ambiguity function analysis for dual-function radar communications using PSK signaling," in *Proc. 52nd Asilomar Conf. Signals Syst. Comput.*, 2018, pp. 900–904.

[20] N. Levanon, "Multifrequency radar signals," in *Proc. Record IEEE Int. Radar Conf.*, 2000, pp. 683–688.

[21] G. Lellouch, A. K. Mishra, and M. Inggs, "Stepped OFDM radar technique to resolve range and Doppler simultaneously," *IEEE Trans. Aerosp. Electron. Syst.*, vol. 51, no. 2, pp. 937–950, Apr. 2015.

[22] C. Shi, F. Wang, M. Sellathurai, J. Zhou, and S. Salous, "Power minimization-based robust OFDM radar waveform design for radar and communication systems in coexistence," *IEEE Trans. Signal Process.*, vol. 66, no. 5, pp. 1316–1330, Mar. 2018.

[23] P. Kumari, N. Gonzalez-Prelcic, and R. W. Heath, "Investigating the IEEE 802.11ad standard for millimeter wave automotive radar," in *Proc. IEEE Veh. Technol. Conf.*, Boston, MA, USA, Sep. 2015, pp. 1–7.

[24] P. Kumari, S. A. Vorobyov, and R. W. Heath, "Adaptive virtual waveform design for millimeter-wave joint communication-radar," *IEEE Trans. Signal Process.*, vol. 68, pp. 715–730, 2020.

[25] A. Tang, S. Li, and X. Wang, "Self-interference-resistant IEEE 802.11ad-based joint communication and automotive radar design," *IEEE J. Sel. Topics Signal Process.*, vol. 15, no. 6, pp. 1484–1499, Nov. 2021.

[26] M. Richards, *Fundamentals of Radar Signal Processing*, 2nd ed. New York, NY, USA: McGrawHill Educ., 2014.

[27] N. Levanon and E. Mozeson, *Radar Signals*. Hoboken, N, USA: Wiley, 2004.

[28] R. Frank, "Polyphase codes with good nonperiodic correlation properties," *IEEE Trans. Inf. Theory*, vol. 9, no. 1, pp. 43–45, Jan. 1963.

[29] B. L. Lewis and F. F. Kretschmer, "A new class of polyphase pulse compression codes and techniques," *IEEE Trans. Aerosp. Electron. Syst.*, vol. AES-17, no. 3, pp. 364–372, May 1981.

[30] R. Senanayake, P. Smith, J. Evans, B. Moran, and R. J. Evans, "A novel joint radar and communications technique based on frequency permutations," in *Proc. IEEE 94th Veh. Technol. Conf. (VTC-Fall)*, 2021, pp. 1–6.

[31] R. Senanayake, P. Smith, T. Han, J. Evans, B. Moran, and R. J. Evans, "Frequency permutations for joint radar and communications," *IEEE Trans. Wireless Commun.*, vol. 21, no. 11, pp. 9025–9040, Nov. 2022.

[32] N. K. Kundu, R. K. Mallik, and M. R. McKay, "Signal design for frequency-phase keying," *IEEE Trans. Wireless Commun.*, vol. 19, no. 6, pp. 4067–4079, Jun. 2020.

[33] H. L. VanTrees, *Detection, Estimation, and Modulation Theory: Radar-Sonar Processing and Gaussian Signals in Noise*. New York, NY, USA: Wiley, 2001.

[34] R. Senanayake, P. Smith, T. Han, J. Evans, W. Moran, and R. Evans, "Frequency permutations for joint radar and communications," 2021, *arXiv:2105.11106*.

[35] T. Han, R. Senanayake, P. Smith, J. Evans, W. Moran, and R. Evans, "Combined radar and communications with phase-modulated frequency permutations," 2021, *arXiv:2107.14396*.

[36] D. Knuth, *The Art of Computer Programming: Sorting and Searching*. vol. 3. Upper Saddle River, NJ, USA: Addison-Wesley, 1973.

[37] R. J. Serfling, "Contributions to central limit theory for dependent variables," *Ann. Math. Stat.*, vol. 39, no. 4, pp. 1158–1175, 1968. [Online]. Available: https://doi.org/10.1214/aoms/1177698240

[38] F. Olver, D. Lozier, R. Boisvert, and C. Clark, *The NIST Handbook of Mathematical Functions*. New York, NY, USA: Cambridge Univ. Press, 2010.

[39] J. G. Proakis and M. Salehi, *Digital Communications*. New York, NY, USA: McGraw-Hill, 2008.

[40] N. L. Johnson, S. Kotz, and N. Balakrishnan, *Continuous Univariate Distributions*, vol. 2. New York, NY, USA: Wiley, 1970.

[41] H. W. Kuhn, *The Hungarian Method for the Assignment Problem*. New York, NY, USA: Wiley, 1955.

TIAN HAN (Graduate Student Member, IEEE) received the B.E. degree in communication engineering from Donghua University, Shanghai, China, in 2018, and the M.E. degree in electrical engineering from the University of Melbourne, Melbourne, Australia, in 2020, where he is currently pursuing the Ph.D. degree with the Department of Electrical and Electronic Engineering. His current research mainly focuses on the joint design of radar and communications.

RAJITHA SENANAYAKE (Member, IEEE) received the B.E. degree in electrical and electronics engineering from the University of Peradeniya, Sri Lanka, and the bachelor's degree in information technology from the University of Colombo, Sri Lanka, in 2009 and 2010, respectively, and the Ph.D. degree in electrical and electronics engineering from the University of Melbourne, Australia, in 2015. She was with the Research and Development Team with Excel Technology, Sri Lanka, from 2009 to 2011 and the Department of Electrical and Computer Systems Engineering, Monash University, Australia, from 2015 to 2016. She is currently a Research Fellow with the Department of Electrical and Electronics Engineering, The University of Melbourne, Australia. Her research interests are in cooperative communications, distributed antenna systems and joint communications and sensing. She is a recipient of the Australian Research Council Discovery Early Career Researcher Award.

PETER SMITH (Fellow, IEEE) received the B.Sc. degree in mathematics and the Ph.D. degree in statistics from the University of London, London, U.K., in 1983 and 1988, respectively. He was with the Telecommunications Laboratories, GEC Hirst Research Centre from 1983 to 1986 and a Lecturer in statistics with the Victoria University of Wellington, New Zealand, from 1988 to 2001. From 2001 to 2015, he worked with the Electrical and Computer Engineering Department, University of Canterbury. In 2015, he joined the Victoria University of Wellington as a Professor of Statistics. He is also an Adjunct Professor in Electrical and Computer Engineering with the University of Canterbury, New Zealand, and an Honorary Professor with the School of Electronics, Electrical Engineering and Computer Science, Queens University Belfast. His research interests include the statistical aspects of design, modeling and analysis for communication systems, especially antenna arrays, MIMO, cognitive radio, massive MIMO, mmWave systems, reconfigurable intelligent surfaces and the fusion of radar sensing and communications. In 2018–2019, he was awarded Visiting Fellowships with the University of Bologna, the University of Bristol and the University of Melbourne. He was was awarded a Distinguished Visiting Fellowship by the U.K.-based Royal Academy of Engineering at Queens University Belfast in 2017.

JAMIE EVANS (Senior Member, IEEE) was born in Newcastle, Australia, in 1970. He received the B.S. degree in physics and the B.E. degree in computer engineering from the University of Newcastle, in 1992 and 1993, respectively, and the M.S. and the Ph.D. degrees in electrical engineering from the University of Melbourne, Australia, in 1996 and 1998, respectively. From March 1998 to June 1999, he was a Visiting Researcher with the Department of Electrical Engineering and Computer Science, University of California at Berkeley, Berkeley. Since returning to Australia in July 1999, he has held academic positions with The University of Sydney, the University of Melbourne, and Monash University. He is currently a Professor of Electrical and Electronic Engineering and a Pro Vice-Chancellor (Education) with the University of Melbourne. His research interests are in communications theory, information theory, and statistical signal processing with a focus on wireless communications networks. He received the University Medal upon graduation from the University of Newcastle and was awarded the Chancellor's Prize for excellence for his Ph.D. thesis.

BILL MORAN (Member, IEEE) received the Ph.D. degree in pure mathematics from the University of Sheffield, U.K. in 1968, and the B.Sc. degree (First Class Hons.) in mathematics from the University of Birmingham in 1965. He has been serving as a Professor of Defence Technology with the University of Melbourne since 2017. From 2014 to 2017, he was Director of the Signal Processing and Sensor Control Group with the School of Engineering, RMIT University, a Professor with the Department of Electrical Engineering, University of Melbourne, Director of Defence Science Institute in University of Melbourne from 2001 to 2014, a Professor of Mathematics from 1976 to 1991, the Head of the Department of Pure Mathematics from 1977 to 1979 and from 1984 to 1986, the Dean of Mathematical and Computer Sciences in 1981, 1982, and 1989 with the University of Adelaide, and the Head of the Mathematics Discipline with the Flinders University of South Australia from 1991 to 1995, the Medical Signal Processing Program from 1995 to 1999 with the Cooperative Research Centre for Sensor Signal and information Processing, and a member of the Australian Research Council College of Experts from 2007 to 2009. He has been a Principal Investigator on numerous research grants and contracts, in areas spanning pure mathematics to radar development, from both Australian and U.S. Research Funding Agencies, including DARPA, AFOSR, AFRL, Australian Research Council, Australian Department of Education, Science and Training, and Defence Science and Technology, Australia. His main areas of research interest are in signal processing both theoretically and in applications to radar, waveform design and radar theory, sensor networks, and sensor management. He also works in various areas of mathematics including harmonic analysis, representation theory, and number theory. He was elected to the Fellowship of the Australian Academy of Science in 1984.

ROB EVANS (Life Fellow, IEEE) was born in Melbourne, Australia, in 1947. He received the B.E. degree in electrical engineering from the University of Melbourne in 1969, and the Ph.D. degree from the University of Newcastle in 1975, followed by Postdoctoral studies with the Laboratory for Information and Decision Systems, MIT, USA, and the Control and Management Department, Cambridge University, U.K. He served on active duty as a Radar-Systems Engineering Officer with the Royal Australian Airforce. In 1977, he took up an academic position with the University of Newcastle. In 1992, he moved to the University of Melbourne. Over the past 45 years, he has served in many leadership roles and on numerous national and international bodies. He has been deeply involved with industry and defence throughout this period. He is currently a Laureate Professor with the University of Melbourne and a Chief Investigator with the Australian Research Council Centre of Excellence for Gravitational Wave Discovery. His research and industry engagement has ranged across many areas, including theory and applications in control systems, industrial electronics, radar systems, signal processing and telecommunications. He is a Fellow of the Australian Academy of Science, a Fellow of the Australian Academy of Technological Sciences and Engineering, a Life Fellow of the Institution of Electrical and Electronic Engineers USA, and a Fellow of the Institution of Engineers Australia.